

Simulation of 24,000 Electrons Dynamics: Real-Time Time-Dependent Density Functional Theory (TDDFT) with the Real-Space Multigrids (RMG)[†]

Jacek Jakowski,^{*,‡,¶} Wenchang Lu,[§] Emil Briggs,[§] David Lingerfelt,[‡] Bobby G. Sumpter,[‡] Panchapakesan Ganesh,[‡] and Jerzy Bernholc[§]

[‡]*Center For Nanophase Materials Sciences, Oak Ridge National Laboratory, Oak Ridge, TN 37831, USA*

[¶]*Computational Sciences and Engineering Division, Oak Ridge National Laboratory, Oak Ridge, TN 37831, USA*

[§]*Department of Physics, North Carolina State University, Raleigh, NC 27695-8202, USA*

E-mail: jakowskij@ornl.gov

Phone: +1 865 574 6174

Abstract

We present the theory, implementation, and benchmarking of a real-time time-dependent density functional theory (RT-TDDFT) module within the RMG code, designed to simulate the electronic response of molecular systems to external perturbations. Our method offers insights into non-equilibrium dynamics and excited states across a diverse range of systems, from small organic molecules to large metallic nanoparticles. Benchmarking results demonstrate excellent agreement with established TDDFT implementations and showcase the superior stability of our time-integration algorithm, enabling long-term simulations with minimal energy drift. The scalability and efficiency of RMG on massively parallel architectures allow for simulations of complex systems, such as plasmonic nanoparticles with thousands of atoms. Future extensions, including nuclear and spin dynamics, will broaden the applicability of this RT-TDDFT implementation,

[†]NOTICE OF COPYRIGHT: This manuscript has been authored by UT-Battelle, LLC under Contract No. DE-AC05-00OR22725 with the U.S. Department of Energy. The United States Government retains and the publisher, by accepting the article for publication, acknowledges that the United States Government retains a non-exclusive, paid-up, irrevocable, worldwide license to publish or reproduce the published form of this manuscript, or allow others to do so, for United States Government purposes. The Department of Energy will provide public access to these results of federally sponsored research in accordance with the DOE Public Access Plan (<http://energy.gov/downloads/doe-public-access-plan>).

providing a powerful toolset for studies of photoactive materials, nanoscale devices, and other systems where real-time electronic dynamics is essential.

1 Introduction

The application of time-dependent electronic structure methods allows for the modeling of molecular response to external perturbations, such as external fields or charged particle beams, providing a wealth of information about physicochemical processes, including non-equilibrium dynamics or electronically excited states.^{1,2} In-depth discussions on the theoretical foundations and practical applications of TDDFT for linear response (LR) in the frequency domain and real-time (RT) in the time domain can be found in Ref. [1].

Historically, one of the first notable implementations of real-time (RT) time-dependent density functional theory (TDDFT) has been reported by Bertsch and Yabana.³ It was based on a real-space grid and the local density approximation (LDA) and applied to benzene. In the following decades, RT-TDDFT took a central role and became the method of choice for applications in spectroscopy,² materials science, solar energy conversion and optoelectronics,⁴ photo- and femto-chemistry, nanoscale plasmonics,⁵ and photocatalysis.^{2,6} Recent examples include (1) electronic circular dichroism, optical UV/VIS and near edge x-ray absorption, Raman scattering spectroscopy,⁷⁻¹¹ (2) nonlinear response of molecular systems in strong fields,¹²⁻¹⁴ (3) charge transfer, photovoltaics, and solar energy conversion, redox reaction,^{2,4,15,16} (4) real-time electron transport and molecular devices,¹⁷⁻¹⁹ (5) ion and electron beam in-

interactions with materials,^{20–24} (6) stopping power,^{25–27} (7) nanoplasmonics and plasmonic catalysis,^{24,28–30} (8) spin and magnetization dynamics.^{31–34}

The real-time TDDFT methodology has been implemented in many electronic structure codes, ranging from quantum chemistry codes utilizing gaussian (NWchem, Gaussian, Q-Chem) and numerical (Siesta, DFTB+) atom-centered basis sets,^{7,35–38} materials science periodic unit cell codes based on plane waves (Qbox/Qball, cp2k, Exciting) and real space grids (Octopus),^{39–42} to finite element codes (DFT-FE).⁴³ Several extensions of real-time electronic structure methods go beyond DFT, including GW methods,^{44,45} BSE,⁴⁶ configuration interaction, coupled clusters,^{47–50} relativistic methods,^{32,33} and coupled electron nuclei dynamics.^{41,51–58}

Compared to frequency-domain linear response (LR) TDDFT, real-time (RT) TDDFT offers several advantages. RT-TDDFT is an initial value boundary problem. Depending on the choice of the initial electronic state and boundary conditions, it is possible to model non-equilibrium charge transfer or electron transport.² RT-TDDFT allows simulation of electronic response to perturbations of arbitrary shape and duration.² Its computational scaling and resource requirements are similar to conventional DFT methods, enabling simulations of large molecular systems not accessible to LR-TDDFT, such as the 20,000-electron system simulations demonstrated with the plane wave Qbox/Qball code.^{40,41,59} However, RT-TDDFT can suffer from peak shifts and inaccurate charge transfer descriptions in non-equilibrium electron dynamics, attributed to the adiabatic DFT approximation and its instantaneous time-dependent densities.^{60–63} Similarly, the coupled electron-nuclei molecular dynamics utilizing instantaneous RT-TDDFT-based electronic structure (so-called Ehrenfest dynamics) follow a "mean field" path and struggle to reproduce the branching into individual reaction pathways expected in the long-time stochastic regime.⁵¹

In general, the choices of representation or basis set used to describe the electronic structure in DFT and TD-DFT offer different advantages and disadvantages. The main approaches include: (1) Localized atomic-like orbitals, which are highly efficient for systems with localized electronic levels, such as molecular systems, but can show unphysical intruder peaks above the ionization threshold, which are artifacts of basis set incompleteness and correspond to transitions to short-lived (unbound) scattering states in the continuum.^{2,7,38,64} (2) Plane waves, which are advantageous for periodic systems due to their natural handling of periodic boundary conditions and uniform accuracy across the unit cell, but are inefficient in dealing with localized and charged systems, and require pseudopotentials and high kinetic energy cutoffs to achieve convergence.^{39–41,65}

Uniformly-spaced grids, which we utilize in this work, are dual to plane waves and thus provide a spatially unbiased basis set that is independent of atomic positions and offers a single accuracy criterion, the grid spacing,

equivalent to the plane-wave kinetic energy cutoff used in plane-wave methods.⁶⁶ However, plane waves offer a natural and very accurate handling of the kinetic energy, while real-space grids require adaptive discretization of the kinetic energy operator to reach the same accuracy as plane waves.⁶⁶ Real-space grid-based methods are also flexible in handling boundary conditions. Both periodic and non-periodic systems can be easily handled, making them versatile for a wide range of systems, from crystals and bulk materials to molecules and surfaces. They also allow for potential simulations of processes involving a free electron ejected by light or a beam particle to a continuum state, electron tunneling from a surface electrode, or the chemistry of a solvated electron.

In contrast to the plane-wave approach, real-space methods are inherently local and can be efficiently implemented on massively parallel computer architectures, with each processor assigned to a different region of space. The RMG code used in this work has been implemented on many highly parallel systems, including exascale supercomputers (Frontier at ORNL and Aurora at ANL), enabling simulations of very large systems consisting of thousands of atoms.

The rest of this paper is organized as follows. The next section 2 discusses the computational methodology, starting with a brief overview of the RMG method and code, followed by theoretical foundations of density matrix propagation based on commutator expansion. The derivations of the commutator expansion are general and can be used beyond the scope of this work. In section 3, we describe the algorithm used here, its implementation, and code optimization for parallel execution. Section 4 presents applications to simulations of optical response of small and medium size molecules (benzene, C₆₀ fullerene and chlorophylls) and compares the results with other electronic structure codes. The last part of this section highlights the scaling and performance of the method in applications to the plasmonic response of large silver nanoparticles. Such systems are of primary importance for photo- and electro-catalysis on plasmonic nanoparticles, and the development of novel sensors based on localized surface plasmon resonance.^{5,6} The paper concludes with a Summary and Outlook section.

2 Methodology

Here we discuss the computational and theoretical background behind the current implementation of real-time TDDFT in the RMG suite of codes, starting with a brief overview of RMG capabilities. Next, we describe the theoretical foundations behind our computational approach in the context of DFT implementation in RMG, including the Magnus expansion and density matrix propagation. The commutator expansion that we present allows to effectively propagate density matrices at the accuracy of exact diagonalization propagation. The derivation of commutator expansion used for den-

sity matrix propagation is general and can be used to formulate other efficient computation schemes beyond the current work, to address such topics as electron dynamics governed by non-Hermitian Hamiltonians, or combined electron-ion dynamics.

2.1 Overview of RMG

RMG (Real-space MultiGrid) is a Density Functional Theory (DFT)-based electronic structure code^{66,67} designed for scalability and high performance on massively parallel supercomputers from its inception. The DFT equations^{68,69} are discretized on real-space grids and adopt the following form:

$$\mathbf{H}[\Psi_n] = \frac{1}{2}\Delta[\Psi_n] + V_{eff}\Psi_n = \varepsilon_n\mathbf{S}[\Psi_n] \quad (1)$$

where \mathbf{H} denotes the Hamiltonian consisting of the kinetic energy and the potential terms, with Ψ_n representing the n^{th} single-electron Kohn-Sham orbital ($n = 1, \dots, N$) and \mathbf{S} being the overlap matrix. A precise, multi-order adaptive discretization is used for the Laplacian, resulting in the same average accuracy as plane-wave codes on the well-known Delta test for 71 elements in the periodic table.^{66,70}

In the simplest one-dimensional (1D) grid case, the Laplacian can be represented as a banded symmetric matrix. Its effect on a vector $\Psi(x)$, discretized on a uniform grid with spacing h , is approximated using the central finite difference formula with $2n + 1$ grid points:

$$\Psi''(x_0) = a_0 \cdot \Psi(x_0) + \sum_{i=1}^n a_i \cdot (\Psi(x_0 + ih) + \Psi(x_0 - ih)) + R_n(h^{2n}) \quad (2)$$

where $R_n(h^{2n})$ is the truncation error and the coefficients $\{a_0, a_1, \dots, a_n\}$ are optimized to make the expression exact for polynomials of degree up to $2n$. In the adaptive discretization used in RMG, a mixture of two Laplacian discretizations, typically of orders 8 and 6, is employed, according to the formula⁶⁶

$$\Psi''_{(new)}(x_0) = (1 + M)\Psi''_{(n)}(x_0) - M\Psi''_{(n-1)}(x_0) \quad (3)$$

where $n = 4$ is used. The value of the non-negative mixing parameter M is optimized by minimizing the error in the Laplacian for a given combination of species using atomic wavefunctions at the beginning of the calculations. The optimization procedure, which is very fast, has been extensively tested and described in the original publication.⁶⁶

The expectation value of an arbitrary operator A is computed using the standard expression:

$$\langle \Psi | A | \Psi \rangle = h \sum_{i,j} \Psi(x_i) \cdot A(x_i, x_j) \cdot \Psi(x_j) \quad (4)$$

The potential term V_{eff} in Eq. 1 contains contributions from the classical electron-ion attraction (with

ions represented by nonlocal or semi-local pseudopotentials), the electron-electron electrostatic repulsion, and an exchange-correlation term, which may include nonlocal contributions (e.g., Hartree-Fock, hybrid, and dispersion functionals). The \mathbf{S} matrix is non-diagonal when ultrasoft pseudopotentials are used.⁷¹

Multigrid preconditioning is used to accelerate convergence by employing a sequence of grids of varying resolutions. The solution is obtained on a grid fine enough to accurately represent both the potentials and the wavefunctions. It is well known that iterations on a given grid level reduce errors with wavelengths comparable to the grid spacing but are less effective for longer wavelengths.^{72,73} Lower-frequency components are handled on auxiliary grids with progressively larger spacings, where remaining errors appear as high-frequency components. This approach ensures rapid convergence. Extensive comparisons show that RMG agrees extremely well⁶⁶ with the plane-wave `Quantum Espresso` code.⁷⁴ The reasons for this close agreement are that plane waves and uniformly spaced real-space grids are duals, and RMG uses very accurate discretizations.

Similarly to plane-wave approaches, pseudopotentials are employed in RMG to represent ionic cores, and both norm-conserving⁷⁵⁻⁷⁷ and ultrasoft⁷⁸ pseudopotentials are supported. Achieving accuracy equivalent to plane-wave codes at grid resolutions similar to plane-wave kinetic energy cutoffs requires adaptive discretization of the kinetic energy operator.⁶⁶ To facilitate large-scale calculations, two approaches are implemented for computing the electronic structure: (i) delocalized orbitals, and (ii) localized orbitals. In the former approach, the orbitals are delocalized across the entire simulation cell, closely analogous to plane-wave calculations, and achieve equivalent accuracy. The latter approach relies on the variational construction of an optimized minimal basis set of atom-centered orbitals localized within a predetermined cutoff radius, reducing overall computational cost and scaling,^{79,80} while reproducing the DFT total energy of the corresponding delocalized-orbitals calculations within 1 *mHa* accuracy.

The RMG code suite consists of several modules. The distribution (<https://github.com/RMGDFT>) contains the code needed to perform DFT calculations for a large number of atoms, and molecular dynamics with DFT forces.⁸¹ An additional non-Equilibrium Green's Function (NEGF) module allows for quantum transport calculations⁸² for nanoscale devices using an optimized localized basis. RMG has been tested on a large number of systems, including supercells of bulk materials containing various impurities, surfaces, interfaces, transition metal oxides, and 2D materials. Its results agree very well with plane-wave calculations and experiment.^{66,67}

RMG runs on Linux, Windows and OS X. It scales from laptops, desktops and clusters to the largest supercomputers, utilizing all CPU cores and GPUs of each cluster or supercomputer node. It also provides large-scale DFT input to the Quantum Monte Carlo

QMCPACK codes,^{83,84} and was part of the QMCPACK Exascale Computing Program project.⁸⁵ The web based interface has been implemented and is available online (<https://tinyurl.com/rmgdft-web>) allowing users to easily generate RMG text input files and automatically populate all control parameters.⁸⁶ The RMG web interface accept atomic coordinate files in several formats. RMG documentation is available at <https://github.com/RMGDFT/rmgdft/wiki>.

2.2 Theory

The real-time Time-Dependent Density Functional Theory (RT-TDDFT) problem, which is central to this paper, can be viewed as a special case within the broader mathematical framework of strongly continuous C_0 semigroups.⁸⁷ While the time-dependent Schrödinger equation, which governs RT-TDDFT, describes unitary propagation in quantum mechanics, the C_0 semigroup framework also applies to non-unitary evolution processes governed by other types of partial differential equations.

For example, C_0 semigroups can describe the solutions to hyperbolic equations, such as the wave equation, which involves reversible wave propagation, as well as parabolic equations like the diffusion and heat equations, which describe irreversible processes. In these cases, the non-unitary nature reflects the dissipative or smoothing effects inherent to these systems.

The C_0 semigroup is a one-parameter family of operators that depends on a time parameter, and the semigroup property (lack of inverse elements) reflects the irreversibility of certain processes, such as diffusion and heat conduction described by parabolic equations. Importantly, the solutions within this framework are often expressed through the direct exponentiation of the semigroup generator, providing a fundamental connection between the mathematical theory and the physical evolution of the system. This connection will also be demonstrated in this manuscript.

2.2.1 Magnus expansion

The exact solution to the time-dependent Schrodinger equation

$$i\hbar \frac{\partial}{\partial t} |\Psi(t, x)\rangle = \hat{H}(x, t) |\Psi(t, x)\rangle, \quad (5)$$

where $\Psi(t, x)$ is the time-dependent wave function subject to the initial conditions $\Psi(0, x) = \Psi_0(x)$ is given by

$$\Psi(t, x) = \mathcal{U}(t) \Psi(0, x), \quad (6)$$

where $\mathcal{U}(t)$ is time evolution operator equal to

$$\mathcal{U}(t) = \exp(\Omega(t)) \quad (7)$$

with prescription for $\Omega(t)$ given by the Magnus expansion^{55,88–90} The $\Omega(t)$ in the time-evolution operator is a time-ordered Hamiltonian integral that can formally be written as $\Omega(t) = -\frac{i}{\hbar} \int_0^t \mathcal{H}(\tau) d\tau$. Here, the symbol $\mathcal{H}(\tau)$ represents time-ordering of the Hamiltonian, $H(t)$, to distinguish it from the usual integration. Following the Magnus expansion, $\Omega(t)$ can be calculated according to

$$\Omega = \Omega_1 + \Omega_2 + \Omega_3 \dots \quad (8)$$

$$\Omega_1 = -\frac{i}{\hbar} \int_0^t H(\tau) d\tau_1 \quad (9)$$

$$\Omega_2 = \frac{1}{2} \int_0^t d\tau_1 \int_0^{\tau_1} d\tau_2 \left[\frac{H(\tau_1)}{i\hbar}, \frac{H(\tau_2)}{i\hbar} \right] \quad (10)$$

$$\Omega_3 = \frac{1}{2} \int_0^t d\tau_1 \int_0^{\tau_1} d\tau_2 \int_0^{\tau_2} d\tau_3 \left(\left[\frac{H(\tau_1)}{i\hbar}, \left[\frac{H(\tau_2)}{i\hbar}, \frac{H(\tau_3)}{i\hbar} \right] \right] + \left[\frac{H(\tau_3)}{i\hbar}, \left[\frac{H(\tau_2)}{i\hbar}, \frac{H(\tau_1)}{i\hbar} \right] \right] \right) \quad (11)$$

with the square bracket denoting the usual commutator $[A, B] = AB - BA$. In all practical implementations, the propagation is performed using a small time step Δt so that the change of the Hamiltonian $H(t)$ within the time step is linear $H(t) = H_0 + t \cdot H'$, where $H_0 = H(0)$, $H_1 = H(\Delta t)$ and $H' = \frac{H_1 - H_0}{\Delta t}$. This allows for analytical integration of the time-ordering commutator expressions, Ω_k in the Magnus expansion, with a first few terms given by

$$\Omega_1 = -\frac{i}{\hbar} \cdot \frac{1}{2} (H_0 + H_1) \Delta t \quad (12)$$

$$\Omega_2 = \frac{1}{12\hbar^2} \Delta t^2 [H_0, H_1] \quad (13)$$

where we assumed that the matrix elements of $H(t)$ change linearly with time from H_0 to H_1 . Here, $\frac{1}{2}(H_0 + H_1)$ in Ω_1 describes an average Hamiltonian between $t = 0$ and $t = \Delta t$.

Inserting expressions for $\Omega_1, \Omega_2 \dots$ into Eq. 7 provides a foundation for formulations of different symplectic and unitary propagation schemes, which are particularly suitable for long-time quantum dynamics simulations. For example, the exact time-evolution operator can be constructed in a spectral form through diagonalization $\mathcal{U}(t) = \mathbf{W} \cdot \exp(\omega) \cdot \mathbf{W}^\dagger$, where ω is a diagonal matrix of eigenvalues of Ω matrix operator and \mathbf{W} are corresponding eigenvectors. Limiting Ω to the first term, Ω_1 , leads to a mid-point propagation scheme. Next, Taylor expansion of $\exp(\Omega_1)$ truncated to the first term (linear in time) leads to the Crank-Nicolson propagation scheme. The Runge-Kutta propagation is not symplectic and as such is not suitable for long-time simulations.

2.2.2 Density matrix propagation

In general, TDDFT equations can be solved using either the state vector approach or density matrix propagation, as the two approaches are equivalent in many

cases. However, the density matrix approach offers several advantages: it naturally allows for the description of mixed thermal states and can be extended to incorporate interactions with the environment via density matrix embedding techniques or Lindblad-type master equations. This makes it particularly useful for exploring non-equilibrium processes and dissipation mechanisms. Furthermore, the density matrix formulation is numerically robust against noise accumulation during long-time dynamics and facilitates efficient parallelization expressed in terms of matrix-matrix operations.

Consider the one-particle density matrix, $P(t) = \sum_i f_i |\Psi_i(t)\rangle \langle \Psi_i(t)|$, where the summation runs over all states and f_i are the corresponding occupation numbers. Its time evolution is governed by the Liouville-von Neumann equation

$$\frac{\partial P(t)}{\partial t} = -\frac{i}{\hbar} (H(t)P(t) - P(t)H(t)). \quad (14)$$

The general expression for the time evolution of density matrices is given by

$$\begin{aligned} P(t) &= \mathcal{U}(t) \cdot P(0) \cdot \mathcal{U}(t)^\dagger \\ &= \exp(\Omega) \cdot P(0) \cdot \exp(\Omega^\dagger) \end{aligned} \quad (15)$$

where $\mathcal{U}(t)$ can be directly obtained in a spectral form from diagonalization of the Ω operator.

We will now show a derivation of an alternative scheme that avoids diagonalization. We start by inserting an auxiliary parameter λ into the time evolution operator for density matrix propagation, Eq. 15,

$$\begin{aligned} P(\lambda) &= \exp(\lambda\Omega) \cdot P(0) \cdot \exp(\lambda\Omega)^\dagger \\ &= \exp(\lambda\Omega) \cdot P(0) \cdot \exp(\lambda\Omega^\dagger), \end{aligned} \quad (16)$$

so that for $\lambda = 1$ the density matrix $P(\lambda) = P(t)$, whereas for $\lambda = 0$ it becomes an initial (unpropagated) density matrix $P(0)$. Here $\Omega \equiv \Omega(t)$ is a time-ordered operator described by Eqs. 8-11. We will now find $P(\lambda = 1)$ from the Taylor expansion of $P(\lambda)$ around $\lambda = 0$

$$P(\lambda) = \sum_{k=0}^{+\infty} \frac{\lambda^k}{k!} P^{(k)}(0). \quad (17)$$

Here, $P^{(k)}(0) = \frac{d^k}{d\lambda^k} P(\lambda) \Big|_{\lambda=0}$. The derivatives $P^{(k)}(\lambda)$ and $P^{(k)}(0)$ are obtained then as follows

$$\begin{aligned} P^{(1)}(\lambda) &= \frac{d}{d\lambda} P(\lambda) = \frac{d}{d\lambda} [\exp(\lambda\Omega) \cdot P(0) \cdot \exp(\lambda\Omega^\dagger)] \\ &= \exp(\lambda\Omega) \cdot [\Omega P(0) + P(0)\Omega^\dagger] \cdot \exp(\lambda\Omega^\dagger) \\ &= \exp(\lambda\Omega) \cdot P^{(1)}(0) \cdot \exp(\lambda\Omega^\dagger) \end{aligned} \quad (18)$$

where $P^{(1)}(0) = [\Omega P(0) + P(0)\Omega^\dagger]$ is identified as

$$\frac{\partial P(t)}{\partial \lambda} \Big|_{\lambda=0}, \text{ and}$$

$$\begin{aligned} P^{(k)}(\lambda) &= \frac{d^k}{d\lambda^k} P(\lambda) = \frac{d}{d\lambda} P^{(k-1)}(\lambda) \\ &= \frac{d}{d\lambda} [\exp(\lambda\Omega) \cdot P^{(k-1)}(0) \cdot \exp(\lambda\Omega^\dagger)] \\ &= \exp(\lambda\Omega) [\Omega P^{(k-1)}(0) + P^{(k-1)}(0)\Omega^\dagger] \exp(\lambda\Omega^\dagger) \\ &= \exp(\lambda\Omega) \cdot P^{(k)}(0) \cdot \exp(\lambda\Omega^\dagger) \end{aligned} \quad (19)$$

where

$$P^{(k)}(0) = \frac{\partial P^{(k-1)}(t)}{\partial \lambda} \Big|_{\lambda=0} = [\Omega P^{(k-1)}(0) + P^{(k-1)}(0)\Omega^\dagger]. \quad (20)$$

When evaluating $P^{(k)}(\lambda)$ we used the fact that $\exp(\lambda\Omega)\Omega = \Omega \exp(\lambda\Omega)$ (commutation) which is consequence of the fact that both Ω and $\exp(\lambda\Omega)$ have the same eigenvectors.

Collecting Eqs. 18-20, inserting them into Eq. 17, and setting $\lambda = 1$ leads to the following expression for the time evolution of density matrix

$$\begin{aligned} P(t) &= P(0) + \{\Omega, P^0\} + \frac{1}{2!} \{\Omega, \{\Omega, P^0\}\} + \dots \\ &\quad + \frac{1}{k!} \{\Omega, \{\dots \{\Omega, P^0\}\}\} + \dots \end{aligned} \quad (21)$$

where $P^0 = P(0)$ and the curly bracket commutator is defined as $\{A, B\} = AB + BA^\dagger$. Eq. 21 can be formally written as

$$P(t) = \exp(\hat{\mathcal{W}}) \cdot P(0) \quad (22)$$

where the action of the superoperator $\hat{\mathcal{W}} = \{\Omega, \cdot\}$ on the density matrix P is defined as $\hat{\mathcal{W}}P \stackrel{\text{def}}{=} (\Omega P + P\Omega^\dagger)$, and $\Omega = -\frac{i}{\hbar} \int_0^t \mathcal{H}(\tau) d\tau$ is a time-ordered Hamiltonian integral obtained from Magnus expansion (Eqs. 8 - 11). The results obtained in Eqs. 22 and 21 emphasize its connection to strongly continuous one-parameter C_0 semigroup,⁹¹ which also describes the time evolution of parabolic (dissipative irreversible processes, such as heat diffusion) and hyperbolic (time-reversible and energy conserving Wave dynamics) differential equations.

The expression in Eq. 21 is derived without constraints on the types of P , H and Ω matrices and is valid for arbitrary P and Ω . It can be used to propagate the density from the times t to $(t + \Delta t)$. To do that we truncate the Magnus expansion to, for example, the first order and make use of Eq. 12. Then $\Omega \approx -\frac{i}{\hbar} \Delta t \cdot \bar{\mathbf{H}}$ where $\bar{\mathbf{H}} = \frac{1}{2} (\mathbf{H}(t) + \mathbf{H}(t + \Delta t))$ is an average Hamiltonian matrix between time t and $(t + \Delta t)$. The resulting

scheme for density matrix propagation is

$$\begin{aligned} \mathbf{P}(t + \Delta t) = & \mathbf{P}(t) - \frac{i}{\hbar} \Delta t [\bar{\mathbf{H}}, \mathbf{P}(t)] - \frac{1}{\hbar^2} \frac{\Delta t^2}{2!} [\bar{\mathbf{H}}, [\bar{\mathbf{H}}, \mathbf{P}(t)]] \\ & + \frac{i}{\hbar^3} \frac{\Delta t^3}{3!} [\bar{\mathbf{H}}, [\bar{\mathbf{H}}, [\bar{\mathbf{H}}, \mathbf{P}(t)]]] + \dots \\ & + \left(\frac{-i}{\hbar}\right)^k \cdot \frac{\Delta t^k}{k!} [\bar{\mathbf{H}}, \dots, [\bar{\mathbf{H}}, [\bar{\mathbf{H}}, \mathbf{P}(t)]]] + \dots \end{aligned} \quad (23)$$

Employing the commutator expansion technique enables the density matrix propagation to be always implemented in terms of matrix-matrix multiplications without a need for diagonalization. Since diagonalization is much slower on massively parallel computers than matrix multiplication, this implementation results in substantial speedup in parallel execution. Because the expression for $\bar{\mathbf{H}}$ includes $\mathbf{H}(t + \Delta t)$ which depends on $\mathbf{P}(t + \Delta t)$ itself, the propagation $\mathbf{P}(t) \rightarrow \mathbf{P}(t + \Delta t)$ needs to be done self-consistently in each iteration, using a more accurate $\bar{\mathbf{H}}$ until the change in $\mathbf{H}(t + \Delta t)$ between iterations is negligible. Self consistency is particularly important for stable long-time propagation (see Ref. ⁵⁵).

2.2.3 Time evolution of the periodic Kohn-Sham state

We now consider time evolution of a periodic Kohn-Sham state, $|\Psi_{n,\mathbf{k}}(x, t)\rangle$, given by

$$i\hbar \frac{\partial}{\partial t} |\Psi_{n,\mathbf{k}}(x, t)\rangle = H_{KS}(x, t) |\Psi_{n,\mathbf{k}}(x, t)\rangle, \quad (24)$$

where $\Psi_{n,\mathbf{k}}(x, t)$ is the position- and time-dependent Bloch wave function for k -point \mathbf{k} and quantum number n . It can be written as a linear combination of N basis functions $\{\phi_\alpha^\eta : \alpha = 1, \dots, N\}$

$$|\Psi_{n,\mathbf{k}}(x, t)\rangle = \sum_{\eta=-\infty}^{+\infty} \sum_{\alpha=1}^N c_{\mathbf{k}}^{n,\alpha}(t) e^{i\mathbf{k}L\eta} |\phi_\alpha^\eta(x)\rangle \quad (25)$$

with η describing the η -th periodic image of the unit cell, L is a lattice constant and $\phi_\alpha^\eta(x) = \phi_\alpha^0(x - L \cdot \eta)$. The time-dependent Kohn-Sham Hamiltonian, $H_{KS}(x, t)$ in Eq. 24, consists of the usual, time-independent DFT hamiltonian, $H_0[\rho(x)]$, and an external perturbation $V(x, t)$, which depends on time and position

$$H_{KS} = H_0(x) + V(x, t). \quad (26)$$

The symbol $\rho(x)$ denotes the electron density

$$\rho(x) = N_k^{-1} \sum_{n,k} f_{n,k} |\Psi_{n,k}|^2 \quad (27)$$

with occupation numbers $f_{n,\mathbf{k}}$. Inserting Eq. 25 into 24 and multiplying on the left with $\langle \phi_{\alpha'}^0 |$ leads to

$$\begin{aligned} i\hbar \sum_{\alpha=1}^N \left(\sum_{\eta=-\infty}^{+\infty} e^{i\mathbf{k}L\eta} \langle \phi_{\alpha'}^0 | \phi_\alpha^\eta \rangle \right) \dot{c}_{\mathbf{k}}^{n,\alpha}(t) = \\ \sum_{\alpha=1}^N \left(\sum_{\eta} e^{i\mathbf{k}L\eta} \langle \phi_{\alpha'}^0 | H | \phi_\alpha^\eta \rangle \right) c_{\mathbf{k}}^{n,\alpha}(t) \end{aligned} \quad (28)$$

where $\dot{c}_{\mathbf{k}}^{n,\alpha}(t) = \frac{\partial}{\partial t} c_{\mathbf{k}}^{n,\alpha}(t)$. The last expression can be written as

$$i\hbar \sum_{\alpha=1}^N S_{\mathbf{k}}^{\alpha',\alpha} \cdot \dot{c}_{\mathbf{k}}^{n,\alpha} = \sum_{\alpha=1}^N H_{\mathbf{k}}^{\alpha',\alpha} \cdot c_{\mathbf{k}}^{n,\alpha}, \quad (29)$$

where

$$S_{\mathbf{k}}^{\alpha',\alpha} = \sum_{\eta=-\infty}^{+\infty} e^{i\mathbf{k}L\eta} \langle \phi_{\alpha'}^0 | \phi_\alpha^\eta \rangle \quad (30)$$

$$H_{\mathbf{k}}^{\alpha',\alpha} = \sum_{\eta=-\infty}^{+\infty} e^{i\mathbf{k}L\eta} \langle \phi_{\alpha'}^0 | H | \phi_\alpha^\eta \rangle \quad (31)$$

or in a matrix form corresponding to a given k -point \mathbf{k} as

$$i\hbar \mathbf{S}_{\mathbf{k}} \dot{\mathbf{C}}_{\mathbf{k}}(t) = \mathbf{H}_{\mathbf{k}} \mathbf{C}_{\mathbf{k}}(t), \quad (32)$$

where $\mathbf{C}_{\mathbf{k}}(t)$ is a matrix composed of column vectors $\{\mathbf{C}_k^1, \mathbf{C}_k^2, \dots, \mathbf{C}_k^N\}$ with each \mathbf{C}_k^i vector containing coefficients $c_k^{i,j}$ of an i -th Kohn-Sham state in Eq. 25; \mathbf{S}_k and \mathbf{H}_k are overlap and hamiltonian matrices with matrix elements given by Eqs. 30 and 31, respectively.

Eq. 32 can be written in an equivalent Liouville-von Neumann form describing density matrix propagation

$$\dot{\mathbf{P}}_{\mathbf{k}}(t) = -\frac{i}{\hbar} (\mathbf{S}_{\mathbf{k}}^{-1} \mathbf{H}_{\mathbf{k}} \mathbf{P}_{\mathbf{k}} - \mathbf{P}_{\mathbf{k}} \mathbf{H}_{\mathbf{k}} \mathbf{S}_{\mathbf{k}}^{-1}). \quad (33)$$

Here, $\mathbf{P}_{\mathbf{k}}$ is a one-particle k -dependent density matrix that describes an N_e electron system ($\text{Tr}[\mathbf{P}_{\mathbf{k}} \mathbf{S}_{\mathbf{k}}] = N_e$). $\mathbf{P}_{\mathbf{k}}$ can be calculated as a sum of the density contribution from each occupied state as $\mathbf{P}_{\mathbf{k}} = \sum_{n=1}^N f_{n,k} \cdot \mathbf{P}_{\mathbf{k},n}$, where $f_{n,k}$ is an occupation number of the n th state in Eq. 32, and $\mathbf{P}_{\mathbf{k},n} = \mathbf{C}_{\mathbf{k}}^n (\mathbf{C}_{\mathbf{k}}^n)^\dagger$ describes its corresponding contribution to the total density matrix, $\mathbf{P}_{\mathbf{k}}$, with the matrix elements given by $P_{\mathbf{k},n}^{\mu,\nu} = c_k^{n,\mu} (\bar{c}_k^{n,\nu})^\dagger$.

Eq. 33 describes propagation of density matrix in a non-orthogonal basis set. It can be obtained through the following steps: (a) direct differentiation of the density matrix expression, $\dot{\mathbf{P}}_{\mathbf{k},n} = \frac{\partial}{\partial t} (\mathbf{C}_{\mathbf{k}}^n \cdot (\mathbf{C}_{\mathbf{k}}^n)^\dagger) = \dot{\mathbf{C}}_{\mathbf{k}}^n (\mathbf{C}_{\mathbf{k}}^n)^\dagger + \mathbf{C}_{\mathbf{k}}^n (\dot{\mathbf{C}}_{\mathbf{k}}^n)^\dagger$, (b) replacing $\dot{\mathbf{C}}_{\mathbf{k}}^n$ and $(\dot{\mathbf{C}}_{\mathbf{k}}^n)^\dagger$ with Eq. 32 multiplied by $\frac{1}{i\hbar} \mathbf{S}^{-1}$ on the left and with its complex conjugation, (c) noting that (\mathbf{S} and \mathbf{H} are hermitian, thus $(\mathbf{S}^{-1} \mathbf{H})^\dagger = \mathbf{H} \mathbf{S}^{-1}$), and finally (d) summing over all occupied states $\dot{\mathbf{P}}_{\mathbf{k}} = \sum_{n=1}^N f_{n,k} \cdot \dot{\mathbf{P}}_{\mathbf{k},n}$.

Eq. 33 can be transformed to an equivalent orthogonal basis form in Eq. 14, whose solution is given by Eq. 23. The orthogonalization can be achieved through factorization of the overlap matrix $\mathbf{S} = \mathbf{L} \mathbf{R}$ with, for example, Löwdin scheme ($\mathbf{L} = \mathbf{R} = \mathbf{S}^{1/2}$), or Cholesky decomposition into lower (\mathbf{L}) and upper tri-

angular (\mathbf{R}) matrices with $\mathbf{L} = \mathbf{R}^\dagger$. Then, the transformation between the orthogonal (\mathbf{o} subscript) and non-orthogonal (\mathbf{n} subscript) basis sets for the Hamiltonian, density, and vectors are given by $\mathbf{H}_\mathbf{n} = \mathbf{L}\mathbf{H}_\mathbf{o}\mathbf{R}$, $\mathbf{H}_\mathbf{o} = \mathbf{L}^{-1}\mathbf{H}_\mathbf{n}\mathbf{R}^{-1}$, $\mathbf{P}_\mathbf{n} = \mathbf{R}^{-1}\mathbf{H}_\mathbf{o}\mathbf{L}^{-1}$, $\mathbf{P}_\mathbf{o} = \mathbf{R}\mathbf{H}_\mathbf{n}\mathbf{L}$, $\mathbf{C}_\mathbf{n} = \mathbf{R}^{-1}\mathbf{C}_\mathbf{o}$, and $\mathbf{C}_\mathbf{o} = \mathbf{R}\mathbf{C}_\mathbf{n}$. See Appendix A for discussion.

Eq. 33 can also be rewritten in the form

$$\dot{\mathbf{P}}_\mathbf{k}(t) = \hat{\mathbf{W}} \bullet \mathbf{P} \quad (34)$$

where the superoperator $\hat{\mathbf{W}} = \{\frac{1}{i\hbar}\mathbf{S}^{-1}\mathbf{H}, \cdot\}$, acts on the density matrix \mathbf{P} and its result is $\hat{\mathbf{W}} \bullet \mathbf{P} = -\frac{i}{\hbar}(\mathbf{S}_\mathbf{k}^{-1}\mathbf{H}_\mathbf{k}\mathbf{P}_\mathbf{k} - \mathbf{P}_\mathbf{k}\mathbf{H}_\mathbf{k}\mathbf{S}_\mathbf{k}^{-1})$. The solution to Eq. 34 can be formally written as

$$\mathbf{P}_\mathbf{k}(t) = \exp(\mathcal{W}) \cdot \mathbf{P}_\mathbf{k}(0), \quad (35)$$

where \mathcal{W} denotes the time-ordered integral of $\hat{\mathbf{W}}$, $\mathcal{W} = \int_0^t \hat{\mathbf{W}} d\tau = \{\mathbf{\Omega}, \cdot\}$, and Magnus expansion (Eqs. 8-11) is used to evaluate $\mathbf{\Omega}$. The action of $\mathcal{W} = \{\mathbf{\Omega}, \cdot\}$ on $\mathbf{P}_\mathbf{k}$ is defined as $\mathcal{W} \bullet \mathbf{P}_\mathbf{k} = \{\mathbf{\Omega}, \mathbf{P}_\mathbf{k}\} = (\mathbf{\Omega}\mathbf{P}_\mathbf{k} + \mathbf{P}_\mathbf{k}\mathbf{\Omega}^\dagger)$. For propagation of density between times t and $(t + \Delta t)$ with the Magnus expansion truncated to first order (see Eqs. 9 and 12), the resulting $\mathbf{\Omega} = \mathbf{\Omega}_1$ and

$$\begin{aligned} \mathbf{\Omega}_1 &= -\frac{i}{\hbar} \int_0^t \mathbf{S}_\mathbf{k}^{-1} \mathbf{H}_\mathbf{k}(\tau) d\tau = -\frac{i}{\hbar} \mathbf{S}_\mathbf{k}^{-1} \int_0^t \mathbf{H}_\mathbf{k}(\tau) d\tau \\ &= (-\frac{i}{\hbar} \Delta t) \cdot \mathbf{S}_\mathbf{k}^{-1} \bar{\mathbf{H}}, \end{aligned} \quad (36)$$

where $\mathbf{S}_\mathbf{k}^{-1}$ is assumed to not depend on time and $\bar{\mathbf{H}}$ describes a mean Hamiltonian, $\bar{\mathbf{H}} = \frac{1}{2}(\mathbf{H}(t) + \mathbf{H}(t + \Delta t))$. The final scheme for the density matrix propagation is

$$\mathbf{P}(t + \Delta t) = \mathbf{P}^0 + \Delta\mathbf{P}^{(1)} + \Delta\mathbf{P}^{(2)} + \Delta\mathbf{P}^{(3)} + \dots \quad (37)$$

where

$$\begin{aligned} \mathbf{P}^0 &= \mathbf{P}(t) \\ \Delta\mathbf{P}^{(1)} &= \{\mathbf{\Omega}_1, \mathbf{P}^0\} = (-\frac{i}{\hbar} \Delta t)(\mathbf{S}^{-1} \bar{\mathbf{H}} \mathbf{P}^0 - \mathbf{P}^0 \bar{\mathbf{H}} \mathbf{S}^{-1}) \\ \Delta\mathbf{P}^{(2)} &= \{\mathbf{\Omega}_1, \Delta\mathbf{P}^{(1)}\} \\ &= \frac{1}{2} (-\frac{i}{\hbar} \Delta t) (\mathbf{S}^{-1} \bar{\mathbf{H}} \Delta\mathbf{P}^{(1)} - \Delta\mathbf{P}^{(1)} \bar{\mathbf{H}} \mathbf{S}^{-1}) \\ &\dots \\ \Delta\mathbf{P}^{(k)} &= \{\mathbf{\Omega}_1, \Delta\mathbf{P}^{(k-1)}\} \\ &= \frac{1}{k} (-\frac{i}{\hbar} \Delta t) (\mathbf{S}^{-1} \bar{\mathbf{H}} \Delta\mathbf{P}^{(k-1)} - \Delta\mathbf{P}^{(k-1)} \bar{\mathbf{H}} \mathbf{S}^{-1}) \end{aligned} \quad (38)$$

For a special case when \mathbf{S} is a unit matrix (for example, periodic systems with k-sampling limited to the Γ point is only), the matrix expression in parenthesis reduces to a conventional commutator $[\bar{\mathbf{H}}, \Delta\mathbf{P}^{(k-1)}]$ and the Eqs.

38 simplify to:

$$\begin{aligned} \mathbf{P}^0 &= \mathbf{P}(t) \\ \Delta\mathbf{P}^{(1)} &= \{\mathbf{\Omega}_1, \mathbf{P}^0\} = (-\frac{i}{\hbar} \Delta t) [\bar{\mathbf{H}}, \mathbf{P}^0] \\ \Delta\mathbf{P}^{(2)} &= \{\mathbf{\Omega}_1, \Delta\mathbf{P}^{(1)}\} = \frac{1}{2} (-\frac{i}{\hbar} \Delta t) [\bar{\mathbf{H}}, \Delta\mathbf{P}^{(1)}] \\ &\dots \\ \Delta\mathbf{P}^{(k)} &= \{\mathbf{\Omega}_1, \Delta\mathbf{P}^{(k-1)}\} = \frac{1}{k} (-\frac{i}{\hbar} \Delta t) [\bar{\mathbf{H}}, \Delta\mathbf{P}^{(k-1)}] \end{aligned} \quad (39)$$

which are identical with Eq. 23. In Appendix A.2 we show that the expressions in Eqs. 37-38 can be obtained by transforming Eq. 33 to an orthogonal basis set in which $\mathbf{S} = \mathbf{1}$, applying the commutator expansion, Eq. 23, and finally, transforming the results back to a non-orthogonal basis set.

3 Implementation

The implementation of real-time TDDFT presented in this paper is based on the open-source multigrid-based software package **RMG**, which can perform electronic structure calculations in real space for molecules, surfaces and periodic solids with thousands of atoms in the unit cell. The current implementation utilizes the so-called length gauge, which is suitable for finite systems. For periodic systems, simulations are more naturally performed in the velocity gauge, which involves perturbations expressed in terms of the current operator rather than the position operator⁹² and will be pursued in future work. The velocity gauge approach requires careful treatment of non-local potentials and pseudopotential operators.⁹³

In this section, we discuss the length-gauge implementation for molecules and large clusters, first presenting RT-TDDFT algorithm as incorporated into **RMG**, and then discuss optimization and parallelization.

3.1 Algorithm

An overview of the RT-TDDFT scheme implemented in **RMG** is shown in Algorithm 1. The computational scheme is based on density matrix propagation (Eqs. 37-38) and involves following major steps:

1. Evaluation of the DFT ground state (lines 1-3).
2. Preparation of the initial conditions and simulation setup (lines 4-8).
3. Time integration (lines 9-29), involving commutator expansion used for exponentiation of the Magnus operator, and the self-consistent Hamiltonian loop.

In the current implementation, we focused on molecular systems. Therefore, the DFT ground state calculations are performed at the Γ point. The occupied

Algorithm 1 Time-Dependent DFT Algorithm

```

/* Ground state DFT calculations: */
1: generate  $|\Psi_k\rangle$  orbitals,  $H_{KS}$  Hamiltonian
2: select active space for TDDFT (Nocc,Nvirt)
3: calculate dipole moment matrices:
    $M_x = \langle \psi_i | x | \psi_j \rangle$ ;  $M_y = \langle \psi_i | y | \psi_j \rangle$ ;  $M_z = \langle \psi_i | z | \psi_j \rangle$ 
    $\vec{M} = [M_x, M_y, M_z]$ 

/* Read in parameters for RT-TDDFT: */
4: Time loop:  $t_0, dt, N_{steps}$ 
5: Convergence criteria:
    $H_{thrs} = 1 \times 10^{-6}$ ;  $dP_{thrs} = 1 \times 10^{-10}$ 
6: External field potential:
    $E_x(t)$ ;  $E_y(t)$ ;  $E_z(t)$ 

/* Prepare initial RT-TDDFT conditions: */
7: Generate initial density matrix:  $P_0$ 
8: Hamiltonian and perturbation matrices:
    $H_0 \leftarrow H_{KS}$ ;  $H_{-1} \leftarrow H_0$ 
    $V = E_x(t) \cdot M_x + E_y(t) \cdot M_y + E_z(t) \cdot M_z$ 

/* Initialization of TDDFT time loop: */
9: for  $j = 1$  to  $N_{steps}$  do
10:    $t = t_0 + j \cdot dt$ 
   /* Extrapolate  $H_1$  from last 2 steps: */
11:    $H_1 = 2H_0 - H_{-1}$ 

   /* Hamiltonian SCF loop: */
12:   Init loop with dummy error:  $H_{err} = 2 \cdot H_{thrs}$ 
13:   while ( $H_{err} > H_{thrs}$ ) do
   /* Magnus expansion: */
14:      $\Omega = (-\frac{i}{\hbar} dt) \frac{1}{2} (H_0 + H_1 + V_{j-1} + V_j)$ 

     /* Commutator expansion: */
15:      $P_1 \leftarrow P_0$ 
16:      $dP_{err} = 2 \cdot dP_{thrs}$ 
17:      $k=0$ 
18:     while ( $dP_{err} > dP_{thrs}$ ) do
19:        $k++$ 
20:        $\Delta P_1 \leftarrow 1/k \cdot (\Omega \cdot \Delta P_1 + \Delta P_1 \cdot \Omega^\dagger)$ 
21:        $P_1 \leftarrow P_1 + \Delta P_1$ 
22:        $dP_{err} = \max(\text{abs}(\Delta P_1))$ 
23:     end while

     /* Hamiltonians update: */
24:     Convergence error:  $H_{err} = \max |H_1 - H_1^{\text{old}}|$ 
25:      $H_1^{\text{old}} \leftarrow H_1$ ;  $H_1 \leftarrow DFT(\rho(P_1))$ 
26:   end while

   /* Analyze results: */
27:   print:  $\vec{\mu}(t) = \vec{\mu}_0 + \text{trace}(P \cdot \vec{M})$ 

   /* Prepare for the next time step: */
28:    $H_{-1} \leftarrow H_0$ ;  $H_0 \leftarrow H_1$ ;  $P_0 \leftarrow P_1$ 
29: end for

```

orbitals and a small number of virtual orbitals are determined self-consistently together with the ground state charge density and potentials. Extra virtual orbitals can be obtained with the non-SCF option in RMG using the fixed ground-state potential. From our tests in section 4, a large number of virtual orbitals is required to obtain a converged optical absorption spectrum. Fortunately, this number is not necessarily proportional to the system size. For example, around the same number of virtual orbitals will generate a converged spectrum for both benzene (30 electrons) and the C_{60} molecule

(240 electrons). The generated Kohn-Sham orbitals $|\psi_i\rangle$ form an orthogonal basis set for density matrix propagation. The overlap matrix in the previous section is an identity matrix. In general, semi-core electrons may need to be included for accurate DFT calculations, typically for heavy elements, such as the Ag nanorods in one of the examples. For some physical problems, the semi-core orbitals do not contribute to the investigated properties and can be excluded from the TDDFT propagation. In these cases, the semi-core orbitals' charge density is fixed during the TDDFT propagation. In section 4, we will show that the absorption spectra extracted from TDDFT simulations for Ag nanorods are nearly identical with or without semi-core orbitals included in the propagation.

A subset of occupied orbitals N_{occ} and a sufficient number of virtual orbitals N_{virt} define the active simulation space (line 2) with the sizes of Hamiltonian and density matrices used in RT-TDDFT equal to $(N_{occ} + N_{virt}) \times (N_{occ} + N_{virt})$. Following the selection of the active space, the dipole operator matrices $M_q = \langle \psi_i | q | \psi_j \rangle$ are formed ($q = x, y, z$) along with the initial density matrix P_0 , and the Hamiltonian matrix $H_0 = \langle \psi_i | H | \psi_j \rangle$. In the current implementation, the external perturbation potential that couples the occupied and virtual states is defined as the electric field dipolar matrix (line 8) $\langle \psi_i | V | \psi_j \rangle$, which depends on a user-defined field strength ($E_x(t), E_y(t), E_z(t)$). In the current implementation, the constant electric field across the molecule is represented by a sawtooth-like potential, with a dipole correction in the vacuum region⁹⁴

The time integration of density matrix propagation is performed within the lines 9-29. The subscript -1, 0 and 1 refer to time stepping and denote, respectively, matrices at times $(t - dt)$, t and $(t + dt)$. Lines 15-23 describe the recursive updates of the propagated density matrix P_1 with the successive ΔP_1 corrections to the density matrix in Eqs. 37-39, until convergence is reached. Convergence of the commutator expansion is achieved when L_∞ norm of ΔP_1 is smaller than a predefined threshold, $dP_{err} < dP_{thrs}$. The propagation of the density matrix from the time t to $(t + dt)$ requires Hamiltonian matrices at both times, H_0 and H_1 , to evaluate the Magnus operator (line 14). However, the H_1 Hamiltonian matrix depends on the propagated density P_1 . To account for this, the density matrix propagation is carried out self-consistently until the difference between the updated H_1 and H_1 from the previous iteration (line 25) is smaller than the predefined threshold, H_{thrs} . During the first iteration at any given time step, the H_1 is extrapolated from H_0 and H_{-1} (line 11).

3.2 Software optimization

The real-time TDDFT module in RMG has been optimized for massively parallel execution on hybrid CPU-GPU computing platforms. The parallelization strategy for the main RMG routines employs a mixed programming model that utilizes MPI, OpenMP, Posix threads,

and optimized libraries (OpenBlas, Scalapack, Magma-GPU). Domain decomposition is used to assign different regions of space to different cores, and a domain may span an entire node, consisting of several CPU cores and GPU accelerators. This greatly reduces the required communications and makes the communication latency more uniform. The orbitals are processed in blocks and do local synchronization within nodes at specific points of the SCF cycle, greatly reducing the need for global synchronization. The RMG code scales nearly linearly to hundreds or more CPU-GPU nodes, depending on problem size, and utilizes all CPU cores and all GPUs in each node.

The numerical operations required to implement the propagator described in Eqs. 37-39 are dominated by matrix-matrix operations in $[\mathbf{H}, \Delta\mathbf{P}^{(k)}]$, which exhibit $O(N^3)$ scaling as the number of basis functions $N = (N_{occ} + N_{virt})$ increases. (The basis functions refer to Kohn-Sham orbitals in this case). While these are computationally intensive, highly optimized BLAS libraries are usually available for performing them on both CPU and GPU architectures. Therefore, the key to achieving good performance is structuring the code to leverage these libraries and, in the case of systems equipped with GPU accelerators, minimizing data transfers between CPU and GPU memory spaces.

The domain decomposition algorithm employed by RMG means that objects of interest, such as the Kohn-Sham wavefunctions, ionic potentials, and charge density are mapped to three-dimensional regions of real space. The domains are distributed over MPI tasks via a Cartesian mesh. Computing resources assigned to each task include a number of host CPU cores per task as well as GPU accelerators for systems equipped with them. Depending on the specific system configuration, GPUs may be shared with several tasks running on the same compute node. This paradigm means that each task has a copy of every basis function but only for a specific region of real space, making computation of matrix elements, such as $\langle \psi_i | H | \psi_j \rangle$, straightforward, although a reduction operation is required to combine the partial results from all MPI tasks. Copies of the resultant square overlap matrices of order N are also needed by all MPI tasks to perform rotations of the orbitals. The same is true of the matrices \mathbf{P} , $\Delta\mathbf{P}$, $\bar{\mathbf{H}}$ from Eqs. 37-39, which presents an interesting optimization problem.

First, while the commutator expansion (Eqs. 37-39) implemented in RMG avoids diagonalization, the resulting density matrix \mathbf{P}_1 is arbitrarily close to the results obtained with exact diagonalization propagator (subject to the convergence threshold dP_{thrs}). The computational cost of the scheme is determined by the cost of this commutator, $[\bar{\mathbf{H}}, \Delta\mathbf{P}]$. Thus, the optimization effort focuses on its minimization. The matrices $\bar{\mathbf{H}}$ and $\Delta\mathbf{P}$ used in RT-TDDFT are usually hermitian and can be decomposed into a sum of symmetric and antisymmetric matrices holding, respectively, the real and imaginary parts, $\bar{\mathbf{H}} = \mathbf{S} + i\mathbf{A}$ and $\Delta\mathbf{P} = \mathbf{S}' + i\mathbf{A}'$. Then,

the complex-complex commutator can be implemented as a sum of four separate real-real commutators

$$[\bar{\mathbf{H}}, \Delta\mathbf{P}] = [\mathbf{S}, \mathbf{S}'] - [\mathbf{A}, \mathbf{A}'] + i[\mathbf{S}, \mathbf{A}'] + i[\mathbf{A}, \mathbf{S}'], \quad (40)$$

each having the same computational cost. However, for pure DFT functionals using only the Γ point, the Hamiltonian matrix $\bar{\mathbf{H}}$ is purely real and symmetric \mathbf{S} , with the imaginary part \mathbf{A} vanishing. This reduces the computational cost by 50% over the full complex-complex commutator, since the commutator expression becomes $[\bar{\mathbf{H}}, \Delta\mathbf{P}] = [\mathbf{S}, \mathbf{S}'] + i[\mathbf{S}, \mathbf{A}']$. Next, both commutators can be implemented via two matrix multiplications, or alternatively as a single matrix multiplication followed by a transpose

$$\begin{aligned} [\mathbf{S}, \mathbf{S}'] &= \mathbf{S}\mathbf{S}' - \mathbf{S}'\mathbf{S} = \mathbf{S}\mathbf{S}' - (\mathbf{S}\mathbf{S}')^T \\ [\mathbf{A}, \mathbf{S}'] &= \mathbf{A}\mathbf{S}' - \mathbf{S}'\mathbf{A} = \mathbf{A}\mathbf{S}' + (\mathbf{A}\mathbf{S}')^T \end{aligned}$$

The computational cost of the matrix multiplications in commutator Eq. 40 increases as $O(N^3)$, while the size of the matrix and hence communication costs between nodes only increase as $O(N^2)$. For small N it is faster for each MPI task to duplicate the work in Eq. 40. As N increases, there will be a point where a distributed matrix multiplication will be faster. The exact value of the crossover depends on both N and the relative speed of communication to computation on a given hardware platform. On ORNL's Frontier, using a node-local multi-GPU matrix multiply routine is faster than a single GPU once N exceeds a few thousands. For a large enough N , a fully distributed matrix multiplication routine will be the best solution, but we have not yet performed calculations in that size range. Eq. 40 may be formulated using only matrix multiplies or a combination of matrix multiplications and transposes. Theoretically, a transpose scales as $O(N^2)$, but in practice, the memory access patterns required by a transpose are so inefficient that it is not a clear win unless suitably optimized routines are available. Both AMD and Nvidia provide such routines via the DGEAM and ZGEAM functions, so the commutator was implemented in that form.

4 Numerical Results

In this section, we benchmark our current RT-TDDFT implementation across molecular systems of varying sizes, focusing on practical aspects: (1) convergence of the results with respect to the number of virtual orbitals, (2) time step choice, (3) conservation of energy and long-term stability, and (4) applicability to large molecular systems. The simulations aim to answer key questions: How does our real-time TDDFT implementation compare with others? What is the stability of time-integration over long time simulations? What is the maximum practical time step and system size for simulations? Addressing these questions helps to un-

derstand its limitations and provides a baseline for its applicability.

The benchmarking covers a range of molecular systems: organic (benzene), inorganic (fullerene), bioorganic (chlorophylls), and metallic (silver nanoparticles). Benzene, a benchmark molecule for real-time TDDFT, is used to compare the stability of our time integration scheme and to perform the time-step stress test. Chlorophylls are used for long simulation length tests, while silver nanoparticles are used for system size tests.

We simulate the optical response to a linearly polarized electric "kick" impulse (Dirac delta) perturbation

$$V^{i,j}(t) = \delta(t) \sum_q^{x,y,z} E_q \cdot \langle \phi_i | \hat{\mu}_q | \phi_j \rangle \quad (41)$$

where $V^{i,j}(t)$ is a matrix element of external electric field perturbation (length gauge) over the set of active orbitals (occupied and virtual), q runs over $\{x, y, z\}$ cartesian coordinates, $\delta(t)$ is a Dirac delta time envelope (kick-type perturbation), and $\hat{\mu}_q = q$ is a dipole moment operator. Photoabsorption spectra are calculated as a sum of Fourier transforms of $\mu_x(t)$, $\mu_y(t)$ and $\mu_z(t)$ obtained from three independent simulations with the kick perturbation potential polarized along x , y , and z directions, respectively. The current implementation is validated against popular real-time TDDFT implementations in NWChem and Q-Chem (localized Gaussian basis sets), and against linear-response TDDFT in Quantum ESPRESSO (QE). Both RMG and QE use similar lattice and mesh setups with Vanderbilt's norm-conserving pseudopotentials.⁷⁸ All calculations were performed with the semi-local PBE functional⁹⁵ due to its computational efficiency. While hybrid functionals, which incorporate a fraction of exact exchange, can provide more accurate descriptions of electronic excitations, their computational cost in real-time TDDFT is significantly higher, with the exchange operator becoming complex-valued.⁵⁵

4.1 Small and medium systems

In this subsection, we discuss the quality of agreement between the absorption spectra for benzene and C₆₀ fullerene generated using the RMG time propagation-based TD-DFT implementation and implementations found in a popular open-source plane wave pseudopotential DFT code (quantum ESPRESSO, QE)^{65,78,96} and an all electron TD-DFT implementation relying on Gaussian-type orbitals as basis functions (NWChem).⁷ All TD-DFT calculations carried out with periodic-boundary conditions (PBC) codes (RMG and QE) rely on a large ($>10 a_0$) vacuum region surrounding the isolated systems to prevent spurious interactions with the periodic images.

Figures 1 and 2 show absorption spectra for benzene and C₆₀ buckminster fullerene for the energy range below the ionization threshold. For NWChem we used

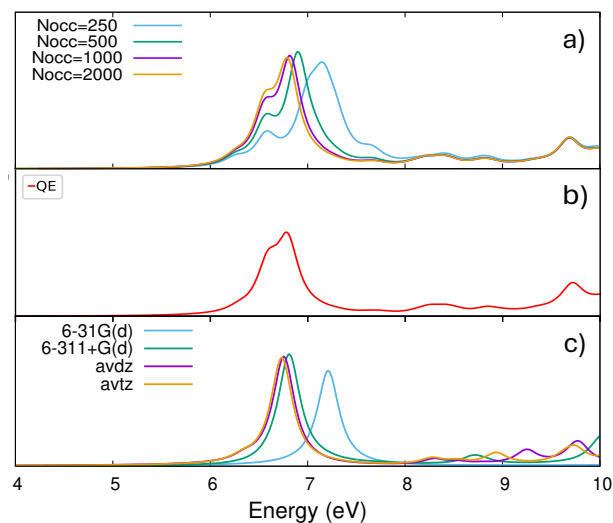


Figure 1: Comparison of benzene dipole oscillator strength (sub-ionization energy region) across the different TD-DFT simulation platforms, with (a) the RMG results using different number of unoccupied orbitals in the expansion space, (b) the quantum ESPRESSO result using analogous plane-wave cutoff to the RMG grid, and well-converged with respect to the depth of the Lanczos recursion employed, and (c) the NWChem result using a typical basis set for TD-DFT calculations of systems comprised of main group elements.

two Pople and two Dunning basis sets: 6-31G(d), 6-311+G(d), aug-cc-pVDZ and aug-cc-pVTZ. For the benzene molecule, a lattice of $36 \times 36 \times 30 (a_0)$ is used with periodic boundary conditions. We used $120 \times 120 \times 100$ real space grid for RMG, and 25 Ry wave function cutoff energy with $120 \times 120 \times 96$ FFT grid for QE. For the C₆₀ fullerene, a $42 \times 42 \times 42 (a_0)$ lattice is used. We employed a $120 \times 120 \times 120$ real space grid for RMG, and 30 Ry wave function cutoff energy with $150 \times 150 \times 150$ FFT grid for QE. Excellent agreement is observed between the line shapes of the photoabsorption spectra produced by the RMG and QE codes using the same boundary conditions and delocalized basis sets. At the same time, a good qualitative agreement is also observed with the all electron NWChem results, where the use of Gaussian-type orbitals imposes the asymptotic decay of the electron density to zero (see fig. 1).

For benzene, the experimentally observed photoabsorption spectrum is mainly comprised of three $\pi \rightarrow \pi^*$ transitions: a very weak band at 4.90 eV (${}^1A_{1g} \rightarrow {}^1B_{2u}$), a stronger (vibronic) band at 6.19 eV (${}^1A_{1g} \rightarrow {}^1B_{1u}$), and a very intense band at 6.96 eV (${}^1A_{1g} \rightarrow {}^1E_{1u}$).⁹⁷ In our simulations, the absorption peak for the (${}^1A_{1g} \rightarrow {}^1E_{1u}$) transition is observed in the range between 6.9 eV and 7.2 eV, depending on the number of basis functions (NWChem) or the number of unoccupied orbitals (RMG) used. The vibronic transition is forbidden by symmetry and does not show up unless

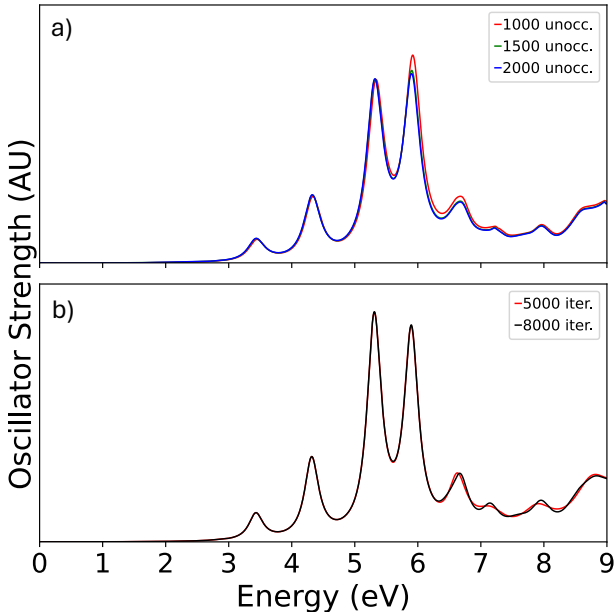


Figure 2: Comparison of C_{60} oscillator strength showing the impact of (a) increasing the number of unoccupied states utilized in the RMG TD-DFT propagation scheme, compared with (b) increasing the number of iterations of the Lanczos recursion-based solver for the analogous system in the quantum ESPRESSO TD-DFT implementation.

the molecular structure of benzene is distorted from D_{6h} symmetry as a result of nuclear motion.

Increasing the number of basis functions in simulations consistently decreases the excitation energy for the ${}^1A_{1g} \rightarrow {}^1E_{1u}$ transition, in accordance with the variational principle applied to the first excited state. Result from NWChem simulations with the smallest 6-31G(d) basis set correspond to RMG results with 250 unoccupied orbitals, both showing the photoabsorption peak near 7.2 eV. The position of the ${}^1A_{1g} \rightarrow {}^1E_{1u}$ transition converges at about 6.9 eV with 1000 unoccupied RMG orbitals, which corresponds to similar NWChem results obtained with aug-cc-pVDZ basis set. Similar convergence with respect to the number of unoccupied orbitals has been observed for RMG simulations of C_{60} fullerene, as shown in Figure 2. For the fewest number of unoccupied orbitals used in RMG (1000), the convergence is nearly complete even at higher energies. Meanwhile, the low-energy region of the spectrum is well converged within the QE implementation with relatively few iterations of the Lanczos algorithm, with higher energy peaks converging much more slowly. Both spectra show a reasonable agreement to the solution-phase experimental spectra.⁹⁸ Thus, in the following RMG simulations we use 1000 unoccupied orbitals as a baseline for RT-TDDFT modeling.

Notably, the QE and RMG results for benzene show a lower intensity absorption peak at 6.6 eV accompanying the main ${}^1A_{1g} \rightarrow {}^1E_{1u}$ transition at 6.9 eV. This

peak corresponds to ${}^1A_{1g} \rightarrow {}^1B_{2u}$ transition and is an artifact of PBE functional.⁹⁹ A similar peak, albeit less pronounced, has also been observed in NWChem simulations using a localized basis set. An in-depth analysis of theoretical benzene spectra and comparison between localized Gaussians and grid based results is provided elsewhere.⁹⁹

Next, we analyzed the sensitivity of the photoabsorption spectra to the size of the time step and the long-term stability of the time-integration algorithm implemented in RMG. The time steps used in the simulations ranged from 0.2 a.u.t. (atomic unit of time) to 5 a.u.t. Figure 3 shows the time-dependence of the instantaneous dipole moment for benzene, conservation of energy, and comparison of the resulting photoabsorption spectra. The simulated photoabsorption spectra for time steps up to $dt=2$ a.u.t. show very good agreement with reference simulations using a time step of 0.2 a.u.t., as seen in Figure 3(d). Clearly, the time integration algorithm is very stable for up to 2 a.u.t., demonstrated by good agreement between time-dependent dipole moments and reference results (black solid line) obtained with a time step of 0.2 a.u.t., as seen in Figure 3(a). For a time step 5.0 a.u.t., the time-integration becomes unstable, with the dipole moment oscillating wildly over time (see olive line in 3.(a)) and loss of energy conservation within the first few time steps (see 3(b)). Figure 3(c) shows conservation of energy for simulations with a time step of 2.0 a.u.t for a 1.8 picoseconds simulation, demonstrating excellent conservation of energy and no observable energy drift throughout the entire simulation time.

Finally, we compared our time integration in RMG with a similar Magnus expansion propagator implemented in NWChem and with the Modified Midpoint Unitary Transform (MMUT) (implemented in NWChem and in Q-Chem).^{7,36} Comparing the time-propagation in NWChem and RMG, we observed a very small energy drift on the order of $10^{-6} E_h$ in NWChem simulations, whereas RMG did not show any noticeable energy drift. It is noteworthy that both NWChem and RMG propagators are based on the time-integration algorithm of density matrices originally proposed by Jakowski and Morokuma.⁵⁵ The main difference in the implementations is that NWChem uses a fixed number of Hamiltonian matrix updates (predictor/corrector iterations), namely two, whereas time propagation in RMG and in Ref. [55] relies on dynamic convergence testing measured as the L_∞ norm of Hamiltonian matrix updates. In RMG, we used a Hamiltonian matrix updates threshold set to 10^{-7} a.u.

As expected, increasing the simulation time step in RMG requires an increased number of Hamiltonian update iterations. For RMG simulations of benzene with time steps of 0.2, 0.5, 1.0, and 2.0 a.u.t., the observed number of Hamiltonian update iterations per time step in the initial non-equilibrium simulation phase were 3, 4, 5, and 9, respectively. In the later simulation phase, the observed number of Hamiltonian updates dropped to 1, 2, 3, and 6 for the time steps of 0.2, 0.5, 1.0, and

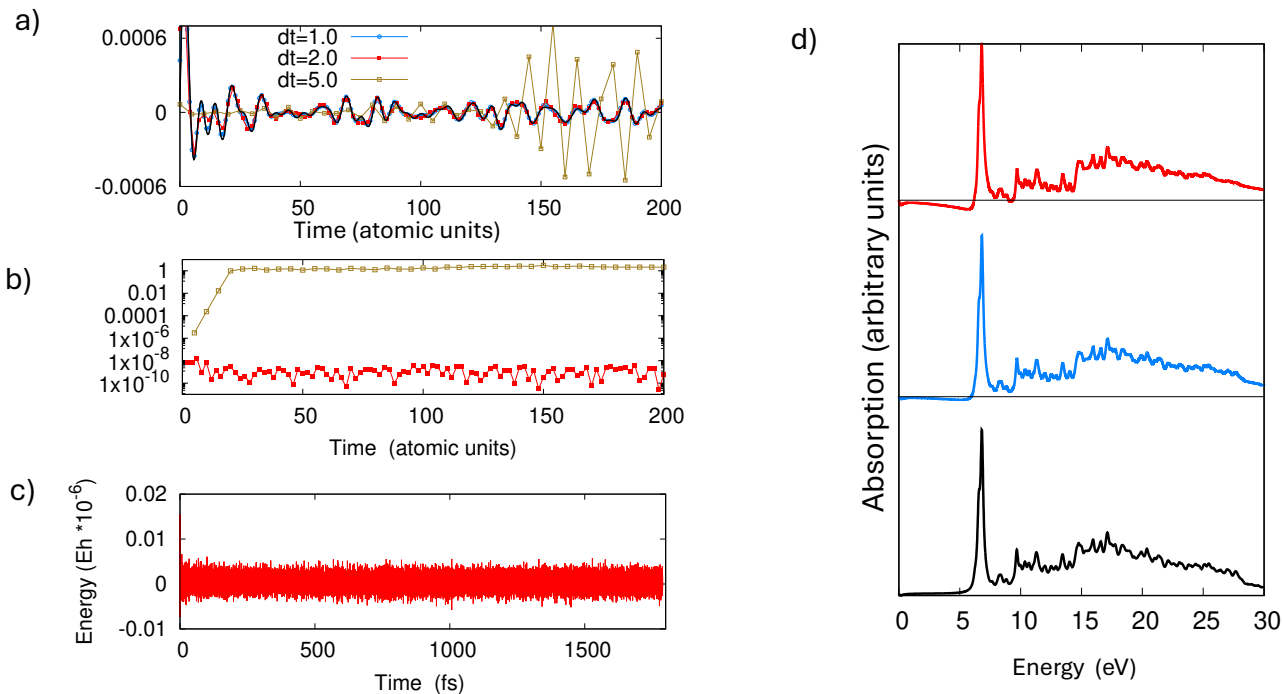


Figure 3: RT-TDDFT results for benzene, showing time-step sensitivity and energy conservation. (a) Time dependence of dipole moment for time steps of 0.2 (solid black line), 1.0, 2.0, and 5.0 a.u.t., with instability and scaled oscillations for $dt = 5.0$ a.u.t. (b) Comparison of energy conservation (logarithmic scale, energy in E_h) up to 200 a.u.t. for $dt = 2.0$ and 5.0 a.u.t., highlighting energy loss at larger time steps. (c) Long time energy conservation for $dt = 2.0$ a.u.t. over 1.8 ps. (d) Photoabsorption spectra for $dt = 0.2, 1.0,$ and 2.0 a.u.t., with $dt = 0.2$ a.u.t. as the reference.

2.0 a.u.t., respectively. These results indicate that for RT-TDDFT simulations of benzene, it is computationally beneficial to increase the time step up to 1.0 a.u.t. However, the computational cost savings are diminished when increasing the time step to 2.0 a.u.t due to the increased number of Hamiltonian updates required.

4.2 Chlorophylls

The molecular systems discussed in the previous section (benzene and C_{60} fullerene) represent spatially compact molecules with high symmetry (point groups D_{6h} and I_h , respectively). Here, we illustrate the application of our RT-TDDFT module implemented in RMG to photoactive chlorophyll molecules, which are asymmetric and significantly larger than benzene and C_{60} fullerene, focusing on long-term stability and comparison with experimental data.

Chlorophylls are bioorganic molecules found in green plants and algae that play a critical role in photosynthesis and the conversion of CO_2 to carbohydrates. Several variations of chlorophylls exist in photosynthetic organisms. Chlorophyll A ($C_{55}H_{72}MgN_4O_5$) is the most abundant of the chlorophylls and is directly involved in converting solar radiation into chemical energy. Chlorophyll B ($C_{55}H_{70}MgN_4O_6$) plays an auxiliary role in

photosynthesis. Both chlorophylls contain a rigid aromatic porphyrin ring with Mg in the center and a floppy hydrocarbon tail. Figure 4(a) shows the molecular structure of chlorophyll B used in the current simulations. The difference between the molecular structures of chlorophyll A and chlorophyll B is that the -CHO group (highlighted within the green dotted oval) is substituted with an - CH_3 group.

The molecular structures of both chlorophylls used for TDDFT simulations were obtained from structure optimization with PBE/6-311+G(d) theory. The RMG input files were generated using RMG web interface⁸⁶ with grid spacing of $0.3 a_0$ and 10 Angstrom vacuum around the chlorophyll molecules to prevent self-interaction with periodic images. The resulting orthorhombic lattice was $(85.9 a_0) \times (43.45 a_0) \times (30.78 a_0)$ for chlorophyll A and $(86.3 a_0) \times (43.3 a_0) \times (32.0 a_0)$ for chlorophyll B. The corresponding values of real-space grids were $288 \times 152 \times 104$ and $288 \times 144 \times 112$, respectively for chlorophyll A and chlorophyll B. Similarly to benzene and C_{60} , periodic boundary conditions were employed. The DFT simulations were performed with the PBE functional and Vanderbilt’s norm-conserving pseudopotentials.⁷⁸

To verify the long-term stability of our time propagation in RMG, we performed 50,000 steps of TDDFT

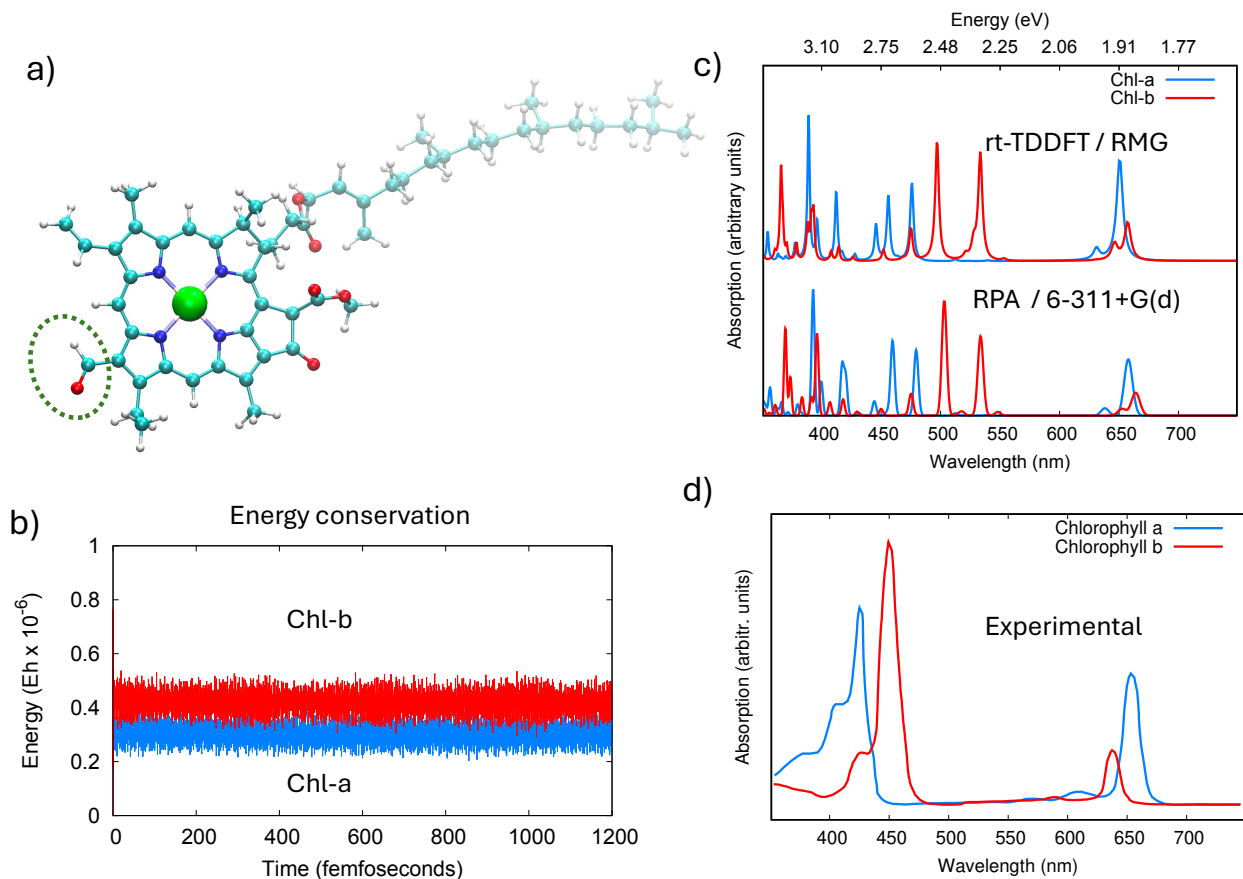


Figure 4: RT-TDDFT simulations of chlorophylls A and B. (a) Molecular structure of chlorophyll B used in the current calculations, with the $-\text{CHO}$ group (highlighted within the green dotted oval) that is substituted by a $-\text{CH}_3$ group in chlorophyll A. (b) Energy conservation for both chlorophylls, calculated relative to the first step after the perturbation potential is turned off. (c) Comparison of photoabsorption spectra for chlorophylls A and B from RMG calculations (denoted as rt-TDDFT/RMG) with linear response TDDFT within Random Phase Approximation (RPA) and with 6-311+G(d) basis set. The RPA results are plotted using Gaussian broadening to mimic experimental line shapes. (d) Experimental photoabsorption spectra of chlorophylls A and B adapted from Ref. [100].

simulations for chlorophyll A and B with a time step of 1.0 a.u.t. and a total simulation time of 1.2 ps. The resulting conservation of energy, optical absorption spectra for both chlorophylls, and comparison with experimental results, are shown in Figure 4(b)-(d). The simulations show excellent conservation of energy with small energy oscillations on the level of $10^{-7} E_h$ and no observable energy drift throughout the 1.2 ps long simulations. The time integration with a time step of 1.0 a.u.t. required about six Hamiltonian matrix updates per simulation time step during the initial, non-equilibrium phase of electron dynamics. It was reduced to about four Hamiltonian updates during the later stages of time propagation. For comparison purposes, we also checked the number of Hamiltonian updates for a simulation with a reference time step of 0.2 a.u.t. The observed Hamiltonian matrix updates were reduced to only two. These results are consistent with those observed for benzene and C_{60} discussed in the previous section.

Figure 4(d) compares RMG spectra from RT-TDDFT (denoted as rt-TDDFT/RMG) with LR-TDDFT spectra within the Random Phase Approximation (RPA) and obtained with the localized Gaussian 6-311+G(d) basis set (denoted as RPA/6-311+G(d)). The agreement between both approaches is excellent. Both result in the same peak positions showing only some intensity differences between both approaches. The experimental spectra, shown in Figure 4(d), are from Ref. [100] and were obtained for chlorophylls dissolved in diethyl ether. They exhibit absorption bands in the blue range (Soret band) with maxima near 428 nm (chl-a) and 453 nm (chl-b), and in the red optical range (Q band) with maxima near 661 nm (chl-a) and 642 nm (chl-b). The simulated spectra show very good agreement with the experimental data, the intensity of the simulated chl-a peak is significantly stronger than that of chl-b. In the blue range, the experimental peaks are clearly composed of several overlapping peaks, which are visible

in the simulated spectra with several peaks within the 350-450 nm range for chl-a and 450-520 nm for chl-b, whereas the corresponding experimental band maxima peak near 428 nm and 453 nm, respectively. We note that the TDDFT simulations are calculated in vacuum and for a single structure of chlorophyll, and as such, neglect thermal motion and broadening. TDDFT simulations by others¹⁰¹ show similar agreement with experimental results, with TDDFT excitation (CAM-B3LYP) energies underestimating experimental Q-band by 0.11 eV (ca. 30 nm) for chl-a and 0.15 eV (ca. 40 nm) for chl-b.

4.3 Plasmonic nanoparticles

Simulations discussed in the previous sections focused on comparing the photoabsorption spectra obtained by RMG with other codes for small and medium-size molecules and benchmarking the effect of time step on the long-term stability of the time integration. Here, we test the feasibility of our TDDFT implementation for simulating electron dynamics in large molecular systems. Specifically, we address the following questions: What is the largest molecular system that can be modeled with the current TDDFT implementation? What are the limiting factors? What is the computational cost per time step for the largest feasible system?

As a model system, we used silver nanorods of increasing size to simulate the longitudinal plasmon resonance peak. Metal nanoparticles have garnered significant attention for their applications in nanoplasmonics and nanophotonics, offering a wide range of applications in sensing, energy, medicine, and imaging.^{102,103} Nanoplasmonics bridges the gap between nanoscale materials science and optical physics, enabling applications in optical filters, waveguides, photonic-circuit components, and sensors.^{28,29,104}

Nanoplasmonic phenomena typically emerge for metallic nanoparticles ranging in size from 2 to 20 nm.¹⁰³ For optimal performance, metal nanoparticles for nanoplasmonic applications should be smaller than approximately 25 nm (the metal’s skin depth), to allow penetration by optical radiation, and larger than about 2 nm, which corresponds to the distance an electron with Fermi velocity travels during a single light oscillation. This size range is significantly smaller than the 400 nm wavelength of visible light.¹⁰² Utilizing such narrow metal films enables surface-enhanced spectroscopy (SES) applications, such as surface-enhanced Raman spectroscopy (SERS).

A silver nanorod exhibits two orthogonal plasmon resonances: a long-wavelength longitudinal plasmon resonance for light polarized along its long axis, and a shorter-wavelength transverse plasmon resonance for light polarized perpendicular to its long axis. Here, we investigate a longitudinal surface plasmon resonance (SPR), focusing on the shift of the SPR frequency as a function of the nanorod size. We used a sequence of increasing size rhombicuboctahedral silver nanorods of

the dimensions $l \times (1.2 \text{ nm}) \times (1.2 \text{ nm})$, where l ranges from 1.6 nm to 20 nm. For all silver nanoparticle cases, the TDDFT active space included the 11 highest energy electrons from each Ag atom, excluding the semi-core electrons (frozen core approximation) and 1000-2000 unoccupied (virtual) orbitals. Overall, we considered nine silver nanorods: Ag₁₈₀, Ag₂₇₀, Ag₃₆₀, Ag₄₅₀, Ag₅₄₀, Ag₆₃₀, Ag₁₀₈₀, Ag₁₆₂₀, and Ag₂₁₆₀ (see Figure 5), with the corresponding number of electrons considered in the TDDFT being 1980, 2970, 3960, 4950, 5940, 6930, 11,880, 17,820, and 23,760, respectively. The RMG calculations used an orthorhombic lattice with the dimensions $L_x \times (44 a_0) \times (44 a_0)$, and $L_x = \{52, 68, 84, 100, 114, 130, 208, 300, 392\}$. The corresponding numbers of real space grid points were $N_x \times 132 \times 132$ with $N_x = \{156, 204, 252, 300, 342, 390, 624, 900, 1176\}$.

All TDDFT calculations for silver nanorods were performed on the Frontier supercomputer at the Oak Ridge Leadership Computing Facility using up to 64 nodes and utilizing all GPUs (8 per Frontier node). The resulting TDDFT spectra obtained with 1.0 a.u.t time step, showing the longitudinal plasmon resonance peak for all nanorods are displayed in Figure 5(b). As expected, we observe a red shift in the position of the plasmon resonance peak with increasing nanoparticle size, with a nearly linear dependence between the particle size and the wavelength corresponding to the plasmon resonance.¹⁰⁵

Table 1 shows the explicit timings for real-time TDDFT simulations on Frontier for three Ag-nanorods: Ag₅₄₀, Ag₁₆₂₀ and Ag₂₁₆₀. Notice that broken sub timing shown for Ag₅₄₀, Ag₁₆₂₀ and Ag₂₁₆₀ does not add up to the total of 110.06 sec, 378.6 sec and 634.3 sec, respectively. The reason is that unless one adds in specific synchronization calls, GPU kernel launches are asynchronous with respect to the host. The synchronization points can cause an overall drop in performance and prevent overlapping computation with data transfer.

For a given system, both the TDDFT and SCF portion of the calculations exhibit $O(N^3)$ scaling per step, but the prefactor for TDDFT steps is smaller. This can be readily seen for the Ag₂₁₆₀ system run on 64 nodes of Frontier (using all of its CPUs and GPUs) where a TDDFT step requires approximately 6.34 seconds while an SCF step requires 108 seconds. The TDDFT simulations for the next size Ag nanorod, namely Ag₂₇₀₀, should be feasible with the current code but have not yet been performed. Calculations on even larger systems present no conceptual problem but may require further optimization of GPU memory usage in order to maintain a similar level of performance.

5 Summary and Outlook

In this work, we presented theory, implementation and benchmarking of a real-time TDDFT (RT-TDDFT) module developed within the RMG code. This approach is designed to model the electronic response of molecu-

Table 1: Explicit real-time TDDFT timings on Frontier supercomputer for 100 TDDFT time steps for selected three Ag-nanorods: Ag₅₄₀, Ag₁₆₂₀ and Ag₂₁₆₀. The number of active basis functions corresponds to the size of density matrix propagated spanning $4d, 5s$ valence orbitals (11 electrons per each Ag atom) plus a set of unoccupied orbitals. The total number of basis function is larger and includes semicore orbitals in addition to valence ones (19 electrons per Ag atom).

System	Ag ₅₄₀ (4.9nm)	Ag ₁₆₂₀ (14.7nm)	Ag ₂₁₆₀ (19.6nm)
Number of active electrons	5,940	17,820	23,760
Number of basis functions (total)	5630	16,890	24,520
Number of basis functions (active)	3470	10,410	15,880
Number of Frontiers nodes used	16	32	64
Hupdate	32.58 (sec)	153.42 (sec)	270.35 (sec)
Rho	31.48 (sec)	124.21 (sec)	162.00 (sec)
Vh	13.08 (sec)	11.50 (sec)	8.74 (sec)
ELDYN	0.86 (sec)	56.37 (sec)	129.40 (sec)
exchange/correlation	13.40 (sec)	11.39 (sec)	9.28 (sec)
Total TD-DFT time	110.06 (sec)	378.6 (sec)	634.3 (sec)
Time for a single TDDFT time step	1.1 (sec)	3.78 (sec)	6.34 (sec)
Time for a single SCF iteration	27.0	124 (sec)	108 (sec)

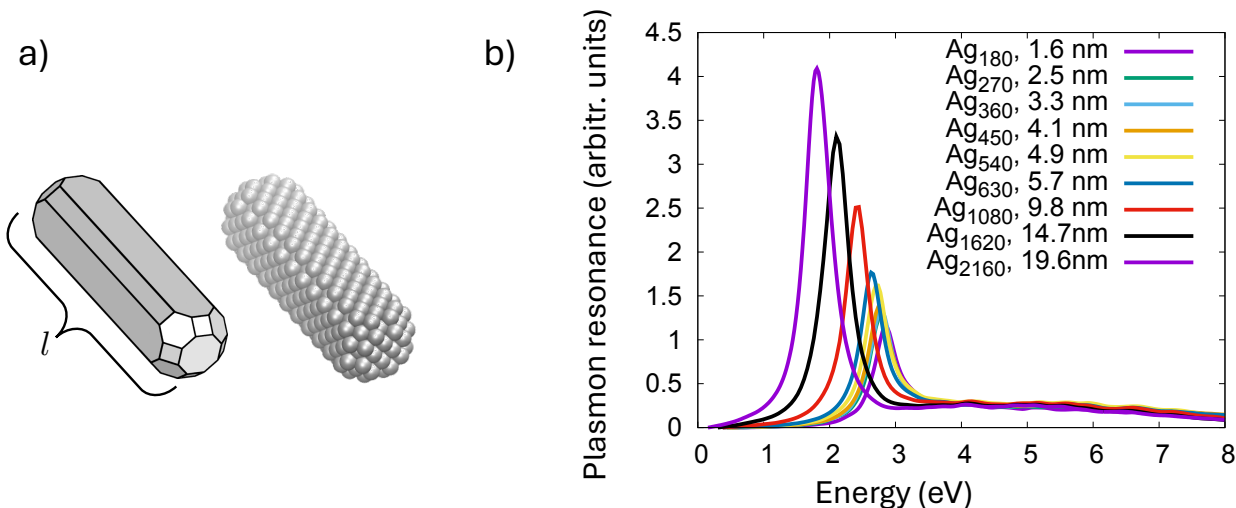


Figure 5: Comparison of longitudinal (i.e., the component along the long axis) dipole oscillator strength normalized with respect to the number of Ag atoms across different lengths (l) of elongated rhombicuboctahedral silver nanorods, showing the expected increase in intensity and redshift in the dipolar longitudinal localized surface plasmon resonance with increasing system size.

lar systems to external perturbations in real-time, providing insights into non-equilibrium dynamics and excited states. Our benchmarking spanned a wide range of molecular systems, from small organic molecules like benzene to large metallic silver nanorods.

The benchmarking demonstrated excellent agreement of RMG results with other TDDFT implementations (e.g., NWChem and Quantum ESPRESSO), validating the accuracy and robustness of our approach. Furthermore, our time-integration algorithm showed superior stability, allowing for long-term simulations with minimal energy drift, even for large time steps.

In addition to electronic dynamics, future extensions of our RT-TDDFT implementation will incorporate nu-

clear motion and spin dynamics, enabling a comprehensive description of coupled electron-nuclear and spin processes. The inclusion of nuclear motion will allow for the study of non-adiabatic dynamics, which are essential for understanding photoinduced processes and energy transfer in molecular systems. Spin dynamics will facilitate the investigation of magnetic properties and spintronics applications, where the interplay between spin and charge degrees of freedom is crucial.

This implementation opens new avenues for exploring electronic dynamics in complex systems, which are computationally challenging for traditional methods. The scalability and efficiency of the RMG code on massively parallel architectures, such as the Frontier supercom-

puter, allow to tackle large-scale problems, including simulations of plasmonic nanoparticles of thousands of atoms. Future work will focus on optimizing the current implementation to push the limits of system size and simulation time further, and exploring more sophisticated electronic structure methods beyond DFT.

Excellent performance and large scale capabilities of RT-TDDFT within RMG provide valuable tools for the study of photoactive materials, nanoscale devices, and other systems where electronic dynamics play a crucial role. The planned extensions include nuclear and spin dynamics, providing insights into the fundamental processes governing complex molecular and material systems.

6 Acknowledgements

This research was conducted at the Center for Nanophase Materials Sciences (CNMS), which is a US Department of Energy, Office of Science User Facility at Oak Ridge National Laboratory. This research used resources of the Oak Ridge Leadership Computing Facility at the Oak Ridge National Laboratory, which is supported by the Office of Science of the U.S. Department of Energy under Contract No. DE-AC05-00OR22725. The development of RMG for exascale computers was supported by DOE's Exascale Computing Project (ECP), Project Number: 17-SC-20-SC, for DFT input to QMCPACK. Computing resources were provided through the Innovative and Novel Computational Impact on Theory and Experiment (INCITE) program and computational resources of the ACCESS (Advanced Cyberinfrastructure Coordination Ecosystem: Services & Support) program through allocation TG-DMR110037.

A Appendix

A.1 Orthogonalization

Rules for Transformation between non-orthogonal and orthonormalized basis set representations.

The non-diagonal overlap matrix $\mathbf{S}_{\mathbf{k}}$ in Eqs. 32 and 33 represents a Gram matrix of inner products over non-orthogonal basis set vectors $\{\phi_i^n\}$, which is positive definite and its matrix elements are $\langle \phi_i^n | \phi_j^n \rangle = S^{i,j}$. The superscript n denotes the non-orthogonality of the basis set. It is often more convenient to work with an equivalent orthonormalized basis set, $\{\phi_i^o\}$, such that $\langle \phi_i^o | \phi_j^o \rangle = \delta_{i,j}$. The transformation from a non-orthogonal basis set $\{\phi_i^n\}$ to an orthonormal one, $\{\phi_i^o\}$, can be achieved by factorization of the overlap matrix $\mathbf{S} = \mathbf{L}\mathbf{R}$, where \mathbf{L} and \mathbf{R} can be obtained in many different ways, for example, using Cholesky or Löwdin factorization, or by directly constructing \mathbf{L} and \mathbf{R} from the eigenvectors of \mathbf{S} . It can be easily checked that the

inverse of \mathbf{S} is given by $\mathbf{S}^{-1} = \mathbf{R}^{-1}\mathbf{L}^{-1}$. Here, the subscript \mathbf{k} is dropped for simplicity.

Considering two orthogonal Bloch states, $|\Psi_i\rangle$ and $|\Psi_j\rangle$, with the corresponding coefficients in a non-orthogonal basis set \mathbf{C}_n^i and \mathbf{C}_n^j , we can write

$$\langle \Psi_i | \Psi_j \rangle = (\mathbf{C}_n^i)^\dagger \cdot \mathbf{S} \cdot \mathbf{C}_n^j = \delta_{i,j} \quad (42)$$

where \mathbf{A}^\dagger denotes the hermitian conjugate of \mathbf{A} . Inserting the factorized overlap matrix into the last expression and using $(\mathbf{A}\mathbf{B})^\dagger = \mathbf{B}^\dagger \cdot \mathbf{A}^\dagger$ gives

$$\begin{aligned} (\mathbf{C}_n^i)^\dagger \cdot \mathbf{S} \cdot \mathbf{C}_n^j &= (\mathbf{C}_n^i)^\dagger (\mathbf{L}\mathbf{L}^{-1}) \cdot \mathbf{S} \cdot (\mathbf{R}^{-1}\mathbf{R})\mathbf{C}_n^j \\ &= ((\mathbf{C}_n^i)^\dagger \mathbf{L}) \cdot (\mathbf{L}^{-1}\mathbf{S}\mathbf{R}^{-1}) \cdot (\mathbf{R}\mathbf{C}_n^j) \\ &= (\mathbf{L}^\dagger \mathbf{C}_n^i)^\dagger \cdot \mathbf{I} \cdot (\mathbf{R}\mathbf{C}_n^j) \\ &= (\mathbf{C}_o^i)^\dagger \cdot \mathbf{I} \cdot \mathbf{C}_o^j = \delta_{i,j} \end{aligned} \quad (43)$$

Here, $\mathbf{L}^\dagger = \mathbf{R}$ (or equivalently, $\mathbf{R}^\dagger = \mathbf{L}$), the diagonal matrix $\mathbf{I} = \mathbf{L}^{-1}\mathbf{S}\mathbf{R}^{-1}$ represents a Gram matrix of the inner product transformed to an orthonormal basis set, and $\mathbf{C}_o^j = \mathbf{R}\mathbf{C}_n^j$ describes the $|\Psi_j\rangle$ vector in orthogonalized basis representation. In fact, inner product of a vector is a special case of a bilinear form and the corresponding transformation between the orthonormal and non-orthogonal basis sets is also valid for Hamiltonian matrix, $\mathbf{H}_o = \mathbf{L}^{-1}\mathbf{H}_n\mathbf{R}^{-1}$, where \mathbf{H}_o and \mathbf{H}_n denote, respectively, the Hamiltonian matrices in orthonormal and non-orthogonal basis sets. Similarly, the inverse transformation from orthogonal to non-orthogonal basis sets are $\mathbf{C}_n = \mathbf{R}^{-1}\mathbf{C}_o$, and $\mathbf{C}_n^\dagger = \mathbf{C}_o^\dagger\mathbf{L}^{-1}$ and $\mathbf{H}_n = \mathbf{L}\mathbf{H}_o\mathbf{R}$.

Following the definition, the density matrix in a non-orthogonal basis is

$$\begin{aligned} \mathbf{P}_n &= \mathbf{C}_n \cdot \mathbf{C}_n^\dagger = (\mathbf{R}^{-1}\mathbf{C}_o) \cdot (\mathbf{C}_o^\dagger\mathbf{L}^{-1}) \\ &= \mathbf{R}^{-1}(\mathbf{C}_o \cdot \mathbf{C}_o^\dagger)\mathbf{L}^{-1} = \\ &= \mathbf{R}^{-1}\mathbf{P}_o\mathbf{L}^{-1} \end{aligned} \quad (44)$$

where $\mathbf{P}_o = \mathbf{C}_o \cdot \mathbf{C}_o^\dagger$ is the density matrix in an orthonormal basis set and the transformation between the orthogonal and non-orthogonal density matrices is $\mathbf{P}_n = \mathbf{R}^{-1}\mathbf{P}_o\mathbf{L}^{-1}$ and $\mathbf{P}_o = \mathbf{R}\mathbf{P}_n\mathbf{L}$. This can be verified by testing whether the trace of the product of the density matrix and of given operator, which is a physical observable, is invariant of the basis set transformation. For example, number of electrons is given by

$$\begin{aligned} N_{el} &= Tr[\mathbf{P}_n\mathbf{S}] \\ &= Tr[(\mathbf{R}^{-1}\mathbf{P}_o\mathbf{L}^{-1}) \cdot (\mathbf{L}\mathbf{R})] \\ &= Tr[\mathbf{R}^{-1}\mathbf{P}_o(\mathbf{L}^{-1}\mathbf{L}) \cdot \mathbf{R}] \\ &= Tr[\mathbf{R}^{-1}\mathbf{P}_o \cdot \mathbf{I} \cdot \mathbf{R}] \\ &= Tr[\mathbf{P}_o \cdot \mathbf{I} \cdot (\mathbf{R} \cdot \mathbf{R}^{-1})] \\ &= Tr[\mathbf{P}_o \cdot \mathbf{I}] \end{aligned} \quad (45)$$

where the following cyclic permutation property of trace has been used $Tr[\mathbf{ABC}] = Tr[\mathbf{BCA}] = Tr[\mathbf{CAB}]$. It

can be similarly verified that $Tr[\mathbf{P}_n \mathbf{H}_n] = Tr[\mathbf{P}_o \mathbf{H}_o]$.

Finally, we can verify that the Liouville-von Neumann equation for the density matrix propagation in an orthogonal basis set, $i\hbar \dot{\mathbf{P}}_o(t) = [\mathbf{H}_o, \mathbf{P}_o]$, transforms to Eq. 33 in a non-orthogonal basis set representation. We start by noticing that the transformation matrices $\mathbf{R}, \mathbf{L}, \mathbf{R}^{-1}$, and \mathbf{L}^{-1} do not depend on time, therefore

$$\begin{aligned} i\hbar \dot{\mathbf{P}}_o(t) &= i\hbar \frac{\partial}{\partial t}(\mathbf{R} \mathbf{P}_n \mathbf{L}) = i\hbar \mathbf{R} \dot{\mathbf{P}}_n \mathbf{L} \\ &= [\mathbf{H}_o, \mathbf{P}_o] = \mathbf{H}_o \mathbf{P}_o - \mathbf{P}_o \mathbf{H}_o \\ &= (\mathbf{L}^{-1} \mathbf{H}_n \mathbf{R}^{-1})(\mathbf{R} \mathbf{P}_n \mathbf{L}) - (\mathbf{R} \mathbf{P}_n \mathbf{L})(\mathbf{L}^{-1} \mathbf{H}_n \mathbf{R}^{-1}) \\ &= \mathbf{L}^{-1} \mathbf{H}_n (\mathbf{R}^{-1} \cdot \mathbf{R}) \mathbf{P}_n \mathbf{L} - \mathbf{R} \mathbf{P}_n (\mathbf{L} \cdot \mathbf{L}^{-1}) \mathbf{H}_n \mathbf{R}^{-1} \\ &= \mathbf{L}^{-1} \mathbf{H}_n \mathbf{P}_n \mathbf{L} - \mathbf{R} \mathbf{P}_n \mathbf{H}_n \mathbf{R}^{-1} \end{aligned} \quad (46)$$

Since in the above expression $i\hbar \dot{\mathbf{P}}_o(t) = i\hbar \mathbf{R} \dot{\mathbf{P}}_n \mathbf{L}$, to obtain Eq. 33, the last expression needs to be multiplied on the left by \mathbf{R}^{-1} and on the right by \mathbf{L}^{-1} , resulting in

$$\begin{aligned} i\hbar \dot{\mathbf{P}}_n &= \mathbf{R}^{-1} \cdot (\mathbf{L}^{-1} \mathbf{H}_n \mathbf{P}_n \mathbf{L} - \mathbf{R} \mathbf{P}_n \mathbf{H}_n \mathbf{R}^{-1}) \cdot \mathbf{L}^{-1} \\ &= (\mathbf{R}^{-1} \mathbf{L}^{-1}) \mathbf{H}_n \mathbf{P}_n (\mathbf{L} \cdot \mathbf{L}^{-1}) \\ &\quad - (\mathbf{R}^{-1} \mathbf{R}) \mathbf{P}_n \mathbf{H}_n (\mathbf{R}^{-1} \mathbf{L}^{-1}) \\ &= \mathbf{S}^{-1} \mathbf{H}_n \mathbf{P}_n - \mathbf{P}_n \mathbf{H}_n \mathbf{S}^{-1} \end{aligned} \quad (47)$$

which is identical to Eq. 33.

A.2 Propagation in non-orthogonal basis set

Here we show the derivation of density matrix propagation in a non-orthogonal basis set. We start from the expression in an orthogonal basis and apply transformation rules to derive the expression in a non-orthogonal basis set.

Consider propagation of the density matrix in a non-orthogonal basis set governed by Eq. 47 which is the same as Eq. 33. For simplicity we denote the non-orthogonal density and Hamiltonian matrices as \mathbf{P}_n and \mathbf{H}_n . These can be transformed to those in an orthogonal basis \mathbf{P}_o and \mathbf{H}_o by a factorization of the overlap matrix $\mathbf{S} = \mathbf{L} \mathbf{R}$. The expressions for transformations between the basis sets are given by $\mathbf{H}_n = \mathbf{L} \mathbf{H}_o \mathbf{R}$, $\mathbf{H}_o = \mathbf{L}^{-1} \mathbf{H}_n \mathbf{R}^{-1}$, and $\mathbf{P}_n = \mathbf{R}^{-1} \mathbf{P}_o \mathbf{L}^{-1}$, and $\mathbf{P}_o = \mathbf{R} \mathbf{P}_n \mathbf{L}$, and $\mathbf{C}_n = \mathbf{R}^{-1} \mathbf{C}_o$, and $\mathbf{C}_o = \mathbf{R} \mathbf{C}_n$.

Denoting $\gamma^k = \frac{1}{k} (-\frac{i}{\hbar} \Delta t)$ and using $\mathbf{S}^{-1} = \mathbf{R}^{-1} \mathbf{L}^{-1}$, the time evolution for density matrix propagation in an orthogonal basis set given by

$$\begin{aligned} \mathbf{P}_o(t + \Delta t) &= \mathbf{P}_o^0 + \Delta \mathbf{P}_o^{(1)} + \Delta \mathbf{P}_o^{(2)} \dots + \Delta \mathbf{P}_o^{(k+1)} + \dots \\ &= \mathbf{P}_o^0 + \gamma^1 [\mathbf{H}_o, \mathbf{P}_o^0] + \gamma^2 [\mathbf{H}_o, \Delta \mathbf{P}_o^{(1)}] \dots \\ &\quad + \gamma^{(k+1)} [\mathbf{H}_o, \Delta \mathbf{P}_o^{(k)}] \end{aligned} \quad (48)$$

and

$$\begin{aligned} \mathbf{P}_n(t + \Delta t) &= \mathbf{R}^{-1} \cdot \mathbf{P}_o(t) \cdot \mathbf{L}^{-1} \\ &= \mathbf{R}^{-1} (\mathbf{P}_o^0 + \Delta \mathbf{P}_o^{(1)} + \Delta \mathbf{P}_o^{(2)} \dots + \Delta \mathbf{P}_o^{(k)} + \dots) \mathbf{L}^{-1} \\ &= \mathbf{P}_n^0 + \Delta \mathbf{P}_n^{(1)} + \Delta \mathbf{P}_n^{(2)} \dots + \Delta \mathbf{P}_n^{(k)} + \dots \end{aligned} \quad (49)$$

where

$$\begin{aligned} \mathbf{P}_o^0 &= \mathbf{P}_o(t) \\ \mathbf{P}_n^0 &= \mathbf{R}^{-1} \cdot \mathbf{P}_o(t) \cdot \mathbf{L}^{-1}, \end{aligned}$$

$$\begin{aligned} \Delta \mathbf{P}_o^{(1)} &= \gamma^1 [\mathbf{H}_o, \mathbf{P}_o^0] \\ &= \gamma^1 (\mathbf{H}_o \mathbf{P}_o^0 - \mathbf{P}_o^0 \mathbf{H}_o) \\ &= \gamma^1 \left((\mathbf{L}^{-1} \mathbf{H}_n \mathbf{R}^{-1})(\mathbf{R} \mathbf{P}_n^0 \mathbf{L}) - (\mathbf{R} \mathbf{P}_n^0 \mathbf{L})(\mathbf{L}^{-1} \mathbf{H}_n \mathbf{R}^{-1}) \right) \\ &= \gamma^1 \left(\mathbf{L}^{-1} \cdot \mathbf{H}_n \mathbf{P}_n^0 \cdot \mathbf{L} - \mathbf{R} \cdot \mathbf{P}_n^0 \mathbf{H}_n \cdot \mathbf{R}^{-1} \right), \end{aligned}$$

$$\begin{aligned} \Delta \mathbf{P}_n^{(1)} &= \mathbf{R}^{-1} \cdot \Delta \mathbf{P}_o^{(1)} \cdot \mathbf{L}^{-1} \\ &= \gamma^1 \mathbf{R}^{-1} \left(\mathbf{L}^{-1} \cdot \mathbf{H}_n \mathbf{P}_n^0 \cdot \mathbf{L} - \mathbf{R} \cdot \mathbf{P}_n^0 \mathbf{H}_n \cdot \mathbf{R}^{-1} \right) \mathbf{L}^{-1} \\ &= \gamma^1 \left(\mathbf{R}^{-1} \mathbf{L}^{-1} \mathbf{H}_n \mathbf{P}_n^0 \mathbf{L} \mathbf{L}^{-1} - \mathbf{R}^{-1} \mathbf{R} \mathbf{P}_n^0 \mathbf{H}_n \mathbf{R}^{-1} \mathbf{L}^{-1} \right) \\ &= \gamma^1 \left(\mathbf{S}^{-1} \cdot \mathbf{H}_n \mathbf{P}_n^0 - \mathbf{P}_n^0 \mathbf{H}_n \cdot \mathbf{S}^{-1} \right), \end{aligned}$$

the k -th order correction

$$\begin{aligned} \Delta \mathbf{P}_o^{(k)} &= \gamma^k [\mathbf{H}_o, \Delta \mathbf{P}_o^{(k-1)}] \\ &= \gamma^k (\mathbf{H}_o \Delta \mathbf{P}_o^{(k-1)} - \Delta \mathbf{P}_o^{(k-1)} \mathbf{H}_o) \\ &= \gamma^k \left((\mathbf{L}^{-1} \mathbf{H}_n \mathbf{R}^{-1})(\mathbf{R} \Delta \mathbf{P}_n^{(k-1)} \mathbf{L}) \right. \\ &\quad \left. - (\mathbf{R} \Delta \mathbf{P}_n^{(k-1)} \mathbf{L})(\mathbf{L}^{-1} \mathbf{H}_n \mathbf{R}^{-1}) \right) \\ &= \gamma^k \left(\mathbf{L}^{-1} \cdot \mathbf{H}_n \Delta \mathbf{P}_n^{(k-1)} \cdot \mathbf{L} - \mathbf{R} \cdot \Delta \mathbf{P}_n^{(k-1)} \mathbf{H}_n \cdot \mathbf{R}^{-1} \right), \end{aligned}$$

and

$$\begin{aligned} \Delta \mathbf{P}_n^{(k)} &= \mathbf{R}^{-1} \cdot \Delta \mathbf{P}_o^{(k)} \cdot \mathbf{L}^{-1} \quad (50) \\ &= \gamma^k \mathbf{R}^{-1} \left(\mathbf{L}^{-1} \mathbf{H}_n \Delta \mathbf{P}_n^{(k-1)} \mathbf{L} - \mathbf{R} \Delta \mathbf{P}_n^{(k-1)} \mathbf{H}_n \mathbf{R}^{-1} \right) \mathbf{L}^{-1} \\ &= \gamma^k \left(\mathbf{R}^{-1} \mathbf{L}^{-1} \mathbf{H}_n \Delta \mathbf{P}_n^{(k-1)} \mathbf{L} \mathbf{L}^{-1} \right. \\ &\quad \left. - \mathbf{R}^{-1} \mathbf{R} \Delta \mathbf{P}_n^{(k-1)} \mathbf{H}_n \mathbf{R}^{-1} \mathbf{L}^{-1} \right) \\ &= \gamma^k \left(\mathbf{S}^{-1} \cdot \mathbf{H}_n \Delta \mathbf{P}_n^{(k-1)} - \Delta \mathbf{P}_n^{(k-1)} \mathbf{H}_n \cdot \mathbf{S}^{-1} \right) \end{aligned}$$

The results obtained here are identical with Eqs. 38 from direct exponentiation of $\exp(\mathcal{W})$, where $\mathcal{W} = \{\Omega, \dots\}$.

References

- (1) Marques, M. A. L., Maitra, N. T., Nogueira, F. M. S., Gross, E. K. U., Rubio, A., Eds. *Fundamentals of Time-Dependent Density Functional*

- Theory*; Lecture Notes in Physics; Springer: Heidelberg, Germany, 2012; Vol. 837.
- (2) Li, X.; Govind, N.; Isborn, C.; A. Eugene De-Prince, I.; Lopata, K. Real-Time Time-Dependent Electronic Structure Theory. *Chem. Rev.* **2020**, *120*, 9951 – 9993.
 - (3) Yabana, K.; Bertsch, G. F. Time-dependent Local-density Approximation in Real Time. *Phys. Rev. B: Condens. Matter Mater. Phys.* **1996**, *54*, 4484–4487.
 - (4) Bhat, V.; Callaway, C. P.; Risko, C. Computational Approaches for Organic Semiconductors: From Chemical and Physical Understanding to Predicting New Materials. *Chem. Rev.* **2023**, *123*, 7498–7547.
 - (5) Zeng, S.; Baillargeat, D.; Ho, H.-P.; Yong, K.-T. Nanomaterials enhanced surface plasmon resonance for biological and chemical sensing applications. *Chem. Soc. Rev.* **2014**, *43*, 3426–3452.
 - (6) DuChene, J. S.; Tagliabue, G.; Welch, A. J.; Cheng, W.-H.; Atwater, H. A. Hot Hole Collection and Photoelectrochemical CO₂ Reduction with Plasmonic Au/p-GaN Photocathodes. *Nano Lett.* **2018**, *18*, 2545–2550.
 - (7) Lopata, K.; Govind, N. Modeling Fast Electron Dynamics with Real-time Time-dependent Density Functional Theory: Application to Small Molecules and Chromophores. *J. Chem. Theory Comput.* **2011**, *7*, 1344 – 1355.
 - (8) Silverstein, D. W.; Govind, N.; Van Dam, H. J.; Jensen, L. Simulating One-Photon Absorption and Resonance Raman Scattering Spectra using Analytical Excited State Energy Gradients within Time-Dependent Density Functional Theory. *J. Chem. Theory Comput.* **2013**, *9*, 5490–5503.
 - (9) Lee, K.-M.; Yabana, K.; Bertsch, G. Magnetic Circular Dichroism in Real-time Time-dependent Density Functional Theory. *J. Chem. Phys.* **2011**, *134*, 144106.
 - (10) De Giovannini, U.; Hübener, H.; Rubio, A. Time-dependent Density Functional Theory Framework for Spin and Time-resolved Angular-resolved Photoelectron Spectroscopy in Periodic Systems. *J. Chem. Theory Comput.* **2017**, *13*, 265–273.
 - (11) Herbert, J. M.; Zhu, Y.; Alam, B.; Ojha, A. K. Time-Dependent Density Functional Theory for X-ray Absorption Spectra: Comparing the Real-Time Approach to Linear Response. *J. Chem. Theory Comput.* **2023**, *19*, 6745 – 6760.
 - (12) Cho, D.; Rouxel, J. R.; Kowalewski, M.; Saurabh, P.; Lee, J. Y.; Mukamel, S. Phase Cycling RT-TDDFT Simulation Protocol for Non-linear XUV and X-ray Molecular Spectroscopy. *J. Phys. Chem. Lett.* **2018**, *9*, 1072 – 1078.
 - (13) Castro, A.; Rubio, A.; Gross, E. K. U. Controlling Single-atom High-harmonic Generation Spectra: A Time-dependent Density-functional Scheme. *Eur. Phys. J. B* **2015**, *88*, 191.
 - (14) Ding, F.; Van Kuiken, B. E.; Eichinger, B. E.; Li, X. An Efficient Method for Calculating Dynamical Hyperpolarizabilities Using Real-Time Time-Dependent Density Functional Theory. *J. Chem. Phys.* **2013**, *138*, 064104.
 - (15) Ranka, K.; Isborn, C. M. Size-dependent errors in real-time electron density propagation. *J. Chem. Phys.* **2023**, *158*, 174102.
 - (16) Jakowski, J.; Irle, S.; Sumpter, B.; Morokuma, K. Modeling charge transfer in fullerene collisions via real-time electron dynamics. *J. Phys. Chem. Lett.* **2012**, *3*, 1536–1542.
 - (17) Schaffhauser, P.; Kümmel, S. Using time-dependent density functional theory in real time for calculating electronic transport. *Phys. Rev. B* **2016**, *93*, 035115.
 - (18) Hod, O.; Rodríguez-Rosario, C. A.; Zelovich, T. Driven Liouville von Neumann Equation in Lindblad Form. *J. Phys. Chem. A* **2016**, *120*, 3278 – 3285.
 - (19) Zelovich, T.; Kronik, L.; Hod, O. Driven Liouville von Neumann Approach for Time-dependent Electronic Transport Calculations in a Nonorthogonal Basis-set Representation. *J. Phys. Chem. C* **2016**, *120*, 15052 – 15062.
 - (20) Lingerfelt, D. B.; Ganesh, P.; Jakowski, J.; Sumpter, B. G. First-Principles Simulation of Beam-Induced Processes Underlying Atomic Manipulation in Electron Microscopes. *Acc. Mater. Res.* **2024**, *5*, 657–686.
 - (21) Lingerfelt, D. .; Ganesh, P.; Sumpter, B.; Jakowski, J. From Ground to Excited Electronic State Dynamics of Electron and Ion Irradiated Graphene Nanomaterials. *Theoretical and Computational Chemistry* **2022**, *21*, 87 – 107.
 - (22) Garashchuk, S.; Huang, J.; Sumpter, B. G.; Jakowski, J. From Classical to Quantum Dynamics of Atomic and Ionic Species Interacting with Graphene and Its Analogue. *Theoretical and Computational Chemistry* **2022**, *21*, 61–86.

- (23) Lingerfelt, D. B.; Ganesh, P.; Jakowski, J.; Sumpter, B. G. Understanding Beam Induced Electronic Excitations in Materials. *J. Chem. Theory and Comput.* **2020**, *16*, 1200–1214.
- (24) Yu, T.; Lingerfelt, D.; Jakowski, J.; Ganesh, P.; Sumpter, B. G. Electron-Beam Induced Molecular Plasmon Excitations and Energy Transfer in Silver Molecular Nanowires. *J. Phys. Chem. A.* **2021**, *125*, 74–87.
- (25) Kononov, A.; Hentschel, T. W.; Hansen, S. B.; Baczewski, A. D. Trajectory sampling and finite-size effects in first-principles stopping power calculations. *npj Comput Mater* **2023**, *9*, 205.
- (26) Schleife, A.; Kanai, Y.; Correa, A. Accurate atomistic first-principles calculations of electronic stopping. *Phys. Rev. B* **2015**, *91*, 014306.
- (27) Ievlev, A. V.; Jakowski, J.; Burch, M.; Iberi, V.; Holland Hysmith, D. C. J.; Sumpter, B. G.; Belianinov, A.; Unocic, R. R.; Ovchinnikova, O. S. Building with Ions: Towards Direct Write of Platinum Nanostructures using In-Situ Liquid Cell Helium Ion Microscopy. *Nanoscale* **2017**, *9*, 12949–12956.
- (28) Ilawe, N. V.; Oviedo, M. B.; Wong, B. M. Dynamics of Long-Range Electronic Excitation Transfer in Plasmonic Nanoantennas. *J. Chem. Theory Comput.* **2017**, *13*, 3442–3454.
- (29) Ilawe, N. V.; Oviedo, M. B.; Wong, B. M. Effect of Quantum Tunneling on the Efficiency of Excitation Energy Transfer in Plasmonic Nanoparticle Chain Waveguides. *J. Mater. Chem. C* **2018**, *6*, 5857–5864.
- (30) Herring, J.; Montemore, M. M. Recent Advances in Real-Time Time-Dependent Density Functional Theory Simulations of Plasmonic Nanostructures and Plasmonic Photocatalysis. *ACS Nanoscience Au* **2023**, *3*, 269–279.
- (31) Ding, F.; Goings, J. J.; Frisch, M. J.; Li, X. Ab Initio Non-Relativistic Spin Dynamics. *J. Chem. Phys.* **2014**, *141*, 214111.
- (32) Goings, J. J.; Kasper, J. M.; Egidi, F.; Sun, S.; Li, X. Real Time Propagation of the Exact Two Component Time-Dependent Density Functional Theory. *J. Chem. Phys.* **2016**, *145*, 104107.
- (33) Konecny, L.; Kadek, M.; Komorovsky, S.; Malkina, O. L.; Ruud, K.; Repisky, M. Acceleration of Relativistic Electron Dynamics by Means of X2C Transformation: Application to the Calculation of Nonlinear Optical Properties. *J. Chem. Theory Comput.* **2016**, *12*, 5823–5833.
- (34) Peralta, J. E.; Hod, O.; Scuseria, G. E. Magnetization Dynamics from Time-Dependent Non-collinear Spin Density Functional Theory Calculations. *J. Chem. Theory Comput.* **2015**, *11*, 3661–3668.
- (35) Xu, Q.; Ben, M. D.; Okyay, M. S.; Choi, M.; Ibrahim, K. Z.; Wong, B. M. Velocity gauge real-time time dependent density functional tight-binding for large scale condensed matter systems. *J. Chem. Theory Comput.* **2023**, *19*, 7989–7997.
- (36) Zhu, Y.; Herbert, J. M. Self-consistent predictor/corrector algorithms for stable and efficient integration of the time-dependent Kohn-Sham equation. *J. Chem. Phys.* **2018**, *148*, 044117.
- (37) Takimoto, Y.; Vila, F. D.; Rehr, J. J. Real-time time-dependent density functional theory approach for frequency-dependent nonlinear optical response in photonic molecules. *J. Chem. Phys.* **2007**, *127*, 154114.
- (38) Hourahine, B.; Aradi, B.; V. Blum, e. a. DFTB+, a software package for efficient approximate density functional theory based atomistic simulations. *J. Chem. Phys.* **2020**, *152*, 124101.
- (39) Castro, A.; Appel, H.; Oliveira, M.; Rozzi, C. A.; Andrade, X.; Lorenzen, F.; Marques, M. A. L.; Gross, E. K. U.; Rubio, A. Octopus: a Tool for the Application of Time-dependent Density Functional. *Theory. Phys. Status Solidi B* **2006**, *243*, 2465–2488.
- (40) W.Draeger, E.; Andrade, X.; Gunnels, J. A.; Bhatele, A.; Schleife, A.; A.Correa, A. Massively parallel first-principles simulation of electron dynamics in materials. *Journal of Parallel and Distributed Computing* **2017**, *106*, 205–214.
- (41) Shepard, C.; Ruiyi Zhou, D. C. Y.; Yao, Y.; Kanai, Y. Simulating electronic excitation and dynamics with real-time propagation approach to TDDFT within plane-wave pseudopotential formulation. *J. Chem. Phys.* **2021**, *155*, 100901.
- (42) Kühne, T.; Iannuzzi, M.; Ben, M. D.; Rybkin, V. V.; Seewald, P.; Stein, F.; Laino, T.; Khaliullin, R. Z.; Schütt, O.; Schiffmann, F. et al. CP2K: An electronic structure and molecular dynamics software package - Quickstep: Efficient and accurate electronic structure calculations. *J. Chem. Phys.* **2020**, *150*, 194103.
- (43) Rufus, N. D.; Kanungo, B.; Gavini, V. Fast and robust all-electron density functional theory calculations in solids using orthogonalized enriched finite elements. *Phys. Rev. B* **2021**, *104*, 085112.

- (44) Dou, W.; Takeshita, T. Y.; Chen, M.; Baer, R.; Neuhauser, D.; Rabani, E. Stochastic Resolution of Identity for Real-Time Second-Order Green's Function: Ionization Potential and Quasi-Particle Spectrum., *J. Chem. Theory Comput.* **2019**, *15*, 6703 – 6711.
- (45) Neuhauser, D.; Gao, Y.; Arntsen, C.; Karshenas, C.; Rabani, E.; Baer, R. Breaking the theoretical scaling limit for predicting quasiparticle energies: the stochastic GW approach. *Phys. Rev. Lett.* **2014**, *17*, 076402.
- (46) Attaccalite, C.; Grüning, M.; Marini, A. Real-time approach to the optical properties of solids and nanostructures: Time-dependent Bethe-Salpeter. *Phys. Rev. B* **2011**, *84*, 245110.
- (47) Luppi, E.; Head-Gordon, M. Computation of high-harmonic generation spectra of H₂ and N₂ in intense laser pulses using quantum chemistry methods and time-dependent density functional theory. *Molecular Physics* **2012**, *110*, 909–923.
- (48) Krause, P.; Klamroth, T.; P., S. Molecular Response Properties from Explicitly Time-dependent Configuration Interaction Methods. *J. Chem. Phys.* **2007**, *127*, 034107.
- (49) Lestrange, P. J.; Hoffmann, M. R.; Li, X. Time-Dependent Configuration Interaction using the Graphical Unitary Group Approach: Nonlinear Electric Properties. *Adv. Quantum Chem.* **2018**, *76*, 195–313.
- (50) Nascimento, D. R.; DePrince, I., A. E. Absorption Spectra from Explicitly Time-Dependent Equation-of-Motion Coupled-Cluster Theory. *J. Chem. Theory Comput.* **2016**, *12*, 5834 – 5840.
- (51) Ghosh, S.; Verma, P.; Cramer, C. J.; Gagliardi, L.; Truhlar, D. G. Combining Wave Function Methods with Density Functional Theory for Excited States. *Chem. Rev.* **2018**, *118*, 7249–7292.
- (52) Abedi, A.; Maitra, N. T.; Gross, E. K. U. Correlated Electron-Nuclear Dynamics: Exact Factorization of the Molecular Wavefunction. *J. Chem. Phys.* **2012**, *137*, 22A530.
- (53) Wu, X.; Wen, S.; Song, H.; Frauenheim, T.; Tretiak, S.; Yam, C.; Zhang, Y. Nonadiabatic molecular dynamics simulations based on time-dependent density functional tight-binding method. *J. Chem. Phys.* **2022**, *157*, 084114.
- (54) Isborn, C. M.; Li, X.; Tully, J. C. Time-dependent density functional theory Ehrenfest dynamics: Collisions between atomic oxygen and graphite clusters. *J. Chem. Phys.* **2007**, *126*, 134307.
- (55) Jakowski, J.; Morokuma, K. Liouville-von Neumann molecular dynamics. *J. Chem. Phys.* **2009**, *130*, 224106.
- (56) J. Jakowski, K. M., S. Irlle Time-dependent quantum dynamical simulations of C₂ condensation under extreme conditions. *Phys. Chem. Chem. Phys.* **2012**, *14*, 6273–6279.
- (57) Kolesov, G.; Grånäs, O.; Hoyt, R.; Vinichenko, D.; Kaxiras, E. Real-Time TD-DFT with Classical Ion Dynamics: Methodology and Applications. *J. Chem. Theory Comput.* **2016**, *12*, 466 – 476.
- (58) Akimov, A. V.; Prezhdo, O. V. The PYXAID Program for Non-Adiabatic Molecular Dynamics in Condensed Matter Systems. *J. Chem. Theory Comput.* **2013**, *9*, 4959 – 4972.
- (59) Gygi, F. Architecture of Qbox: A scalable first-principles molecular dynamics code. *IBM J. Res. Dev.* **2008**, *52*, 137–144.
- (60) Provorse, M. R.; Habenicht, B. F.; Isborn, C. M. Peak-Shifting in Real-Time Time-Dependent Density Functional Theory. *J. Chem. Theory Comput.* **2015**, *11*, 4791 – 4802.
- (61) Luo, K.; Fuks, J. I.; Maitra, N. T. Studies of Spuriously Shifting Resonances in Time-dependent Density Functional Theory. *J. Chem. phys.* **2016**, *145*, 044101.
- (62) Fuks, J. I.; Elliott, P.; Rubio, A.; Maitra, N. T. Dynamics of Charge-transfer Processes with Time-dependent Density Functional Theory. *J. Phys. Chem. Lett.* **2013**, *4*, 735– 739.
- (63) Fuks, J. I.; Maitra, N. T. Charge Transfer in Time-dependent Density-functional Theory: Insights from the Asymmetric Hubbard Dimer. *Phys. Rev. A* **2014**, *89*, 062502.
- (64) Epifanovsky, E.; Gilbert, A. T. B.; Feng, X.; Lee, J.; Mao, Y.; Mardirossian, N.; Pokhilko, P.; White, A. F.; Coons, M. P.; Dempwolff, A. L. et al. Software for the frontiers of quantum chemistry: An overview of developments in the Q-Chem 5 package. *The Journal of Chemical Physics* **2021**, *155*, 084801.
- (65) Ge, X.; Binnie, S. J.; Rocca, D.; Gebauer, R.; Baroni, S. turboTDDFT 2.0-Hybrid functionals and new algorithms within time-dependent density-functional perturbation theory. *Comput. Phys. Commun.* **2014**, *185*, 2080–2089.

- (66) Briggs, E. L.; Lu, W.; Bernholc, J. Adaptive finite differencing in high accuracy electronic structure calculations. *npj Comput. Mater.* **2024**, *10*, 17.
- (67) Briggs, E. L.; Sullivan, D. J.; Bernholc, J. Real-space multigrid-based approach to large-scale electronic structure calculations. *Physical Review B* **1996**, *54*, 14362–14375.
- (68) Hohenberg, P.; Kohn, W. Inhomogeneous electron gas. *Phys. Rev.* **1964**, *136*, B864–B871.
- (69) Kohn, W.; Sham, L. J. Self-consistent equations including exchange and correlation effects. *Phys. Rev.* **1965**, *140*, A1133 – A1138.
- (70) Lejaeghere, K.; Bihlmayer, G.; Björkman, T.; Blaha, P.; Blügel, S.; Blum, V.; Caliste, D.; Castelli, I. E.; Clark, S. J.; Corso, A. D. et al. Reproducibility in density functional theory calculations of solids. *Science* **2016**, *351*, aad3000.
- (71) Vanderbilt, D. Soft self-consistent pseudopotentials in a generalized eigenvalue formalism. *Phys. Rev. B* **1990**, *41*, 7892.
- (72) Brandt, A.; Livne, O. E. *Multigrid Techniques: 1984 Guide with Applications to Fluid Dynamics, Revised Edition*; Society for Industrial and Applied Mathematics, 2011.
- (73) Briggs, W. L.; Henson, V. E.; McCormick, S. F. *A Multigrid Tutorial, Second Edition*, 2nd ed.; Society for Industrial and Applied Mathematics, 2000.
- (74) Giannozzi, P.; Andreussi, O.; Brumme, T.; Bunau, O.; Nardelli, M. B.; Calandra, M.; Car, R.; Cavazzoni, C.; Ceresoli, D.; Cococcioni, M. et al. Advanced capabilities for materials modelling with Quantum ESPRESSO. *Journal of Physics: Condensed Matter* **2017**, *29*, 465901.
- (75) Hamann, D. R. Generalized norm-conserving pseudopotentials. *Phys. Rev. B* *40*, 2980 **1989**, *40*, 2980.
- (76) Bachelet, G. B.; Hamann, D. R.; Schlüter, M. Pseudopotentials that work: From H to Pu. *Phys. Rev. B* **1982**, *26*, 4199.
- (77) Kleinman, L.; Bylander, D. M. Efficacious Form for Model Pseudopotentials. *Phys. Rev. Lett.* **1982**, *48*, 1425.
- (78) Garrity, K. F.; Bennett, J. W.; Rabe, K. M.; Vanderbilt, D. Pseudopotentials for high-throughput DFT calculations. *Computational Materials Science* **2014**, *81*, 446–452, [Online; accessed 2023-11-13].
- (79) Fattebet, J.-L.; Bernholc, J. Towards grid-based $O(N)$ density-functional theory methods: Optimized nonorthogonal orbitals and multigrid acceleration. *Phys. Rev. B* **2000**, *62*, 1713–1722.
- (80) Bernholc, J.; Briggs, E. L.; Bungaro, C.; Nardelli, M. B.; Fattebet, J. L.; Rapcewicz, K.; Roland, C.; Schmidt, W. G.; Zhao, Q. Large-scale applications of real-space multigrid methods to surfaces, nanotubes, and quantum transport. *Physica Status Solidi (b)* **2000**, *217*, 685–701.
- (81) Lu, W.; Briggs, E.; Bernholc, J. RMG: an Open Source code for electronic structure calculations and modeling of materials and molecules. (Version 6.0), 2024; <https://github.com/RMGDFT/rmgdft>.
- (82) Lu, W.; Meunier, V.; Bernholc, J. Nonequilibrium Quantum Transport Properties of Organic Molecules on Silicon. *Phys. Rev. Lett.* **2005**, *95*, 206805.
- (83) Kim, J.; Baczewski, A. D.; Beaudet, T. D.; Benali, A.; Bennett, M. C.; Berrill, M. A.; Blunt, N. S.; Borda, E. J. L.; Casula, M.; Ceperley, D. M. et al. QMCPACK: an open source ab initio quantum Monte Carlo package for the electronic structure of atoms, molecules and solids. *Journal of Physics: Condensed Matter* **2018**, *30*, 195901.
- (84) Kent, P. R. C.; Annaberdiyev, A.; Benali, A.; Bennett, M. C.; Landinez Borda, E. J.; Doak, P.; Hao, H.; Jordan, K. D.; Krogel, J. T.; Kylänpää, I. et al. QMCPACK: Advances in the development, efficiency, and application of auxiliary field and real-space variational and diffusion quantum Monte Carlo. *The Journal of Chemical Physics* **2020**, *152*, 174105.
- (85) Alexander, F.; Almgren, A.; Bell, J.; Bhattacharjee, A.; Chen, J.; Colella, P.; Daniel, D.; DeSlippe, J.; Diachin, L.; Draeger, E. et al. Exascale applications: skin in the game. *Philosophical Transactions of the Royal Society A: Mathematical, Physical and Engineering Sciences* **2020**, *378*, 20190056.
- (86) Lu, W.; Briggs, E.; Bernholc, J. RMG Input File Generator. <https://rmgdft-rmgwebinterface-main-y6jk8h.streamlit.app/>, (Version 1.0), 2024; <https://tinyurl.com/rmgdft-web>.
- (87) Engel, K.-J.; Nagel, R. *A Short Course on Operator Semigroups*; Universitext Series; Springer, 2000.

- (88) Magnus, W. On the exponential solution of differential equations for a linear operator. *Commun. Pure Appl. Math.* **1954**, *7*, 649.
- (89) Oteo, A.; Ros, J. From time-ordered products to Magnus expansion. *J. Math. Phys.* **2000**, *41*, 3268.
- (90) Casas, F. Sufficient conditions for the convergence of the Magnus expansion. *J. Phys. A: Math. Theor.* **2007**, *40*, 15001.
- (91) Hairer, H.; Lubich, C.; Wanner, G. *Geometric Numerical Integration. Structure-preserving Algorithms for Ordinary Differential Equations*; Springer Series in Computational Mathematics; Springer, 2000.
- (92) Ditter, E.; Mattiat, J.; Lubner, S. The position operator problem in periodic calculations with emphasis on theoretical spectroscopy. *Phys. Chem. Chem. Phys.* **2023**, *25*, 14672.
- (93) Mattiat, J.; Lubner, S. Comparison of Length, Velocity, and Symmetric Gauges for the Calculation of Absorption and Electric Circular Dichroism Spectra with Real-Time Time-Dependent Density Functional Theory. *J. Chem. Theory Comput.* **2022**, *18*, 5513 – 5526.
- (94) Bengtsson, L. Dipole correction for surface supercell calculations. *Phys. Rev. B* **1999**, *59*, 12301–12304.
- (95) Perdew, J. P.; Burke, K.; Ernzerhof, M. Generalized Gradient Approximation Made Simple. *Phys. Rev. Lett.* **1996**, *77*, 3865–3868.
- (96) Giannozzi, P.; Baroni, S.; Bonini, N.; Calandra, M.; Car, R.; Cavazzoni, C.; Ceresoli, D.; Chiarotti, G. L.; Cococcioni, M.; Dabo, I. et al. QUANTUM ESPRESSO: a modular and open-source software project for quantum simulations of materials. *Journal of Physics: Condensed Matter.* **2009**, *21*, 395502.
- (97) Feng, R.; Cooper, G.; Brion, C. Dipole (e,e) spectroscopic studies of benzene: quantitative photoabsorption in the UV, VUV and soft X-ray regions. *Journal of Electron Spectroscopy and Related Phenomena* **2002**, *123*, 199–209, Determination of cross-sections and momentum profiles of atoms, molecules and condensed matter.
- (98) Menéndez-Proupin, E.; Delgado, A.; Montero-Alejo, A. L.; De La Vega, J. G. The absorption spectrum of C₆₀ in n-hexane solution revisited: Fitted experiment and TDDFT/PCM calculations. *Chem. Phys. Lett.* **2014**, *593*, 72–76.
- (99) Montserrat, R.; and Alexandre B. Rocha, R. R. O. Total absorption spectrum of benzene aggregates obtained from two different approaches. *Journal of Molecular Modeling* **2024**, *30*, 66.
- (100) Lichtenthaler, H. K.; Buschmann, C. Chlorophylls and Carotenoids: Measurement and Characterization by UV-VIS Spectroscopy. *Current Protocols in Food Analytical Chemistry* **2001**, *1*, F4.3.1–F4.3.8.
- (101) Milne, B. F.; Toker, Y.; Rubio, A.; Nielsen, S. B. Unraveling the Intrinsic Color of Chlorophyll. *Angew. Chem.* **2015**, *127*, 2198–2201.
- (102) Stockman, M. I. Nanoplasmonics: The physics behind the applications. *Physics Today* **2011**, *64*, 39–44.
- (103) Stockman, M. I. Nanoplasmonics: past, present, and glimpse into future. *Optics Express* **2011**, *19*, 22029–22106.
- (104) Goncalves, M. R.; Minassian, H.; Melikyan, A. Plasmonic resonators: fundamental properties and applications. *J. Phys. D: Appl. Phys.* **2020**, *53*, 443002.
- (105) Sorensen, L. K.; Khrennikov, D. E.; Gerasimov, V. S.; Ershov, A. E.; Polyutov, S. P.; Karpov, S. V.; ; Ågren, H. Nature of the Anomalous Size Dependence of Resonance Red Shifts in Ultrafine Plasmonic Nanoparticles. *J. Chem. Phys. C* **2022**, *126*, 16804–16814.